Journal of Building Engineering 104 (2025) 112273

Contents lists available at ScienceDirect

Journal of Building Engineering

journal homepage: www.elsevier.com/locate/jobe

Enhancing the fracture performance of cementitious composites through synergistic integration of graphene with polyolefin and polyvinyl alcohol fibres

Shahzad Ashraf, Magdalena Rucka *

Department of Mechanics of Materials and Structures, Faculty of Civil and Environmental Engineering, Gdańsk University of Technology, Narutowicza 11/12, 80-233, Gdańsk, Poland

ARTICLE INFO

Keywords:
Fracture characteristics
Durability
Graphene nanoplatelets
Polyolefin fibre
Polyvinyl alcohol fibre
Hybrid fibre reinforced concrete
Acoustic emission (AE)

ABSTRACT

Polyvinyl alcohol fibre (PVA) and polyolefin fibre (PO) are utilized in engineering cementitious composites (ECCs) due to their excellent crack-bridging capabilities, durability, ductility and energy absorption capacity. However, their combined effects on crack propagation mechanism, especially when combined with nano-reinforcement, remain underexplored. Recently, graphene nanoplatelets (GNPs) have emerged as promising nano-reinforcement in composite materials for enhancing the mechanical, thermal, and crack propagation resistance. Based on this premise, this study investigates the synergistic effects of GNPs combined with single and hybrid fibre reinforcement of PO-PVA at varying dosages (0.1 vol%, 0.3 vol%, and 0.6 vol%), aiming to improve the fracture performance of cementitious composites. Three-point bending tests were conducted using the AE technique to monitor crack initiation and propagation, allowing an in-depth analysis of crack evolution characteristics. By employing various AE parameters and advanced AE analysis methods, this research captures critical insights into microcracking events, fracture mechanisms, and failure modes in single and hybrid- PO-PVA fibre-reinforced composites containing GNPs. The research identifies the most beneficial concrete mix designs that significantly enhances interfacial bonding, microstructural integrity and fracture performance. Furthermore, the hybridisation of PVA-PO-GNPs leads to a notable shift in the dominant fracture mode towards shear cracks. This study findings are expected to provide novel insights into the optimization of FRC enhanced with nanomaterials, paving the way for innovative applications in advancing high-performance engineering structures with improved fracture resistance.

1. Introduction

Concrete is one of the most widely used building materials in the world, valued for its strength, durability, resilience, energy efficiency, and affordability. However, due to its brittle nature and limited tensile strength, it is prone to cracking and significant deformation under mechanical and environmental loading [1,2]. Any significant cracks allow aggressive chemicals to infiltrate the structure, significantly reducing the water tightness of concrete and thus deteriorating its durability [3,4]. Therefore, it is particularly important to study the fracture process mechanism in concrete material and to precisely detect early-stage cracking for structural safety. Steel reinforcement has been a mainstay of construction practice for the past few decades due to its excellent tensile strength,

* Corresponding author.
E-mail addresses: shahzad.ashraf@pg.edu.pl (S. Ashraf), magdalena.rucka@pg.edu.pl (M. Rucka).

https://doi.org/10.1016/j.jobe.2025.112273
Received 14 November 2024; Received in revised form 5 February 2025; Accepted 4 March 2025
Available online 5 March 2025

but it also enhances the structural integrity of concrete, enabling it to withstand high loads and extreme conditions. However, the inherent susceptibility to corrosion poses a serious threat to the durability of reinforced concrete (RC) structures [5,6]. Furthermore, the use of reinforcing bars in concrete increases the overall dead load of the structure and limits its design flexibility, requiring additional cost and design considerations [7]. Fibre reinforcement (FRC) concrete has emerged as a promising alternative in modern construction practice addressing the limitations associated with traditional reinforcement solutions by enhancing overall performance and increasing the resistance to early crack propagation. It offers several advantages such as improved post-cracking performance, greater energy dissipation capacity, enhanced corrosion resistance, and improved architectural aesthetics, making it superior to conventional strengthening methods [8]. Numerous researchers have demonstrated that incorporating various types of fibres including steel fibres [9–11], synthetic fibres [12,13], glass fibres [14], carbon fibres [15,16], and polymer fibres [17–19] into cement-based composites provides an efficient technique for improving fibre-matrix integrity, ductility, shear strength, energy absorption capacity and crack resistance properties in quasi-brittle materials.

This ultimately strengthens and enhances the durability of concrete materials against corrosive environments. Among the fibres, the use of polyvinyl alcohol (PVA) fibre and polyolefin (PO) fibre in fibre-reinforced cementitious composites (FRCCs) has received considerable attention in recent years [20,21]. PVA, a hydrophilic synthetic fibre, has been widely used in cementitious materials to mitigate shrinkage cracking and enhance ductility owing to its high tensile strength and elastic modulus compared to polypropylene and natural fibres, along with its good dispersion, high aspect ratio, and excellent corrosion resistance [22,23]. In contrast, polyolefin (PO) possesses hydrophobic properties that rely on a mechanical interaction for bonding between fibre and cementitious matrix rather than a chemical reaction. This unique characteristic offers several benefits, including improved bending strength, better post-cracking behaviour, and enhanced resistance to corrosion and harsh alkaline environments [24]. To meet the growing demand for sustainable and resilient infrastructure for society, several researchers are making significant efforts to develop innovative approaches to optimize the mechanical properties, durability, cost-effectiveness and overall performance of green infrastructure systems. One promising approach involves incorporating a mix of different fibre types in optimal ratios [25,26], replacing steel fibres with more affordable synthetic alternatives [27], and combining fibre reinforcement with supplementary cementitious materials (SCMs) [28]. Xu et al. [29] investigated the optimal dosage to achieve a synergistic effect in hybrid fibre reinforcement with three types of fibres: cellulose, polyvinyl alcohol, and polyolefin. Their experimental results revealed that combining 1.5 kg/m^3 cellulose fibres with 1.0 kg/m^3 polyvinyl alcohol fibres resulted in the most effective enhancement in the mechanical performance of the concrete. Shaaban et al. [30] examined the effectiveness of hybrid fibre (PVA and PP) reinforcement, up to 2.5 %, in mitigating cracks in RC beams, with and without shear reinforcement. They concluded that the incorporation of a small amount (0.75 % each) of PVA-PP hybrid fibres along with stirrups resulted in superior ductility and shear strength compared to beams without fibres or higher fibre content. Recent advances in nanotechnology have introduced carbon nano-materials into FRCCs to promote the formation of a denser microstructure and 3D bonding at the fibre-matrix interface. This 3D structure improves the interfacial bonding and mechanical properties between the fibre and the cementitious matrix, thereby controlling cracking and preventing the brittle failure of concrete [31,32]. Graphene nanoplatelets (GNPs) are emerging as prominent nanofiller-reinforcing materials in nanocomposites, particularly due to their effective reinforcing capabilities in fibre-reinforced composites. They inhibit the voids in the interfacial transition zone at the nano-scale level to strengthen the matrix, facilitate the load transfer efficiency and increase the overall toughness of the composites [33]. Recently, many studies have been published to investigate the synergistic effects of GNPs on FRCCs, which can significantly improve their mechanical [34,35], thermal [36] and interlaminar [37] properties as a result of the addition of low doses of GNPs. Gurbuz et al. [28] studied the effectiveness of nano-graphite platelet (NGP)-treated PVA fibres in engineered cementitious composites (ECC). They observed that NGP treatment increased the hydrophobicity of the fibre and roughened its surface, which allowed better bonding to the matrix and improved crack-bridging capabilities.

Concrete is a heterogeneous material that undergoes a multi-scale failure process when loaded. During the failure process, microcracks develop in the matrix and as the load increases, these microcracks grow and expand into macrocracks. Therefore, it takes advanced monitoring methods to fully investigate the damage mechanisms and fracture performance in composite materials under stress. Acoustic emission (AE) is one of the non-destructive testing (NDT) methods that has emerged as a valuable real-time technology for identifying crack initiation and progression in FRCCs [38,39], nano-based cementitious composites [40], strain-hardening cement-based composites [26] and rubberized concrete [41]. The various statistical AE parameters including ring-down counts, hits, signal strength, rise time, amplitude, AE energy, and duration, were used to investigate the crack propagation behaviour and failure modes in concrete structures under different loading conditions [42]. Other parameters related to the frequency of AE signals, such as peak frequency, frequency centroid, and partial power, can provide insight into the specific types of damage occurring in FRC [43]. In addition, collected raw AE parameters can also be analysed to identify different types of damage and failure mechanisms in composite structures. For example, the relationship between RA (rise time/amplitude) and AF (counts/duration) has been effectively employed to distinguish between flexural failure and shear failure [44,45]. Li et al. [46] used the AE technique to differentiate between various cracking modes in PVA fibre-reinforced calcium sulphoaluminate cement mortar by correlating AE parameters such as counts, energy, average frequency (AF), and rise time (RA) values. They observed that matrix cracking generated spikes in AE counts and energy at the first peak load. After peak load, fibre pull-out events maintained a high AE activity rate, indicating better crack resistance due to the bridging effects of the PVA fibres. Ashraf et al. [38] used a combined AE and DIC methods to investigate the fracture evolution of polyolefin and steel fibre concrete beams during three-point bending tests. Their parameter-based AE findings revealed that the addition of polyolefin fibres to plain concrete resulted in a higher number of hits with lower amplitudes, reflecting delayed and distributed microcracking. This pattern reflected delayed and distributed microcracking, indicating improved fibre-matrix bonding and crack-bridging effects. Moreover, fluctuations in the b-value trend demonstrated the transition from micro to macrocracks, indicating enhanced resistance between the fibres and the matrix.

However, improvements are still needed to enhance the interfacial bonding properties between the fibres and the cementitious matrix. Polyvinyl alcohol (PVA) fibres, due to their hydrophilic nature, can result in weaker chemical adhesion, while polyolefin (PO) fibres, due to their hydrophobic nature, can also result in weaker interfacial bonding with the matrix. This study proposes the use of graphene nanoplatelets (GNPs) as nano-reinforcement within the cementitious matrix, alongside PVA and PO fibres. The integration of GNPs is expected to significantly improve the fibre-matrix bonding strength by enhancing mechanical interlocking, surface energy, and load transfer capabilities. This approach aims to address the limitations of PVA and PO fibres in achieving strong interfacial bonds, thereby enhancing fracture resistance and overall composite performance under mechanical loading.

2. Research significance and implications

Recent studies have explored the fracture behaviour of cement-based composites reinforced with graphene nanoplatelets (GNPs), polyolefin (PO), and polyvinyl alcohol (PVA) fibres. However, there is limited understanding of how GNPs specifically affect crack propagation mechanisms and interact with different fibre types as nano-reinforcements. This research addresses this gap by investigating the synergistic effects of GNPs combined with single and hybrid PO-PVA fibres on the fracture behaviour of cementitious matrix under flexural loading, using the acoustic emission (AE) method. This study provides practical insights for optimizing GNPs-integrated FRC structural designs, promoting more resilient and sustainable infrastructure while reducing maintenance requirements and environmental impact.

3. Material and methods

3.1. Materials and mixture proportions

All specimens had the same mix design, containing CEM I 42.5R cement (532 g), water (266 g), sand 0/2 mm (1064 g), aggregate 2/8 mm (1470 g), graphene nanoplatelets (GNPs at 0.025 % of the cement weight), and super-plasticizer (0.025 % of the cement weight). The particle size distribution of 0/2 mm sand and 2/8 mm aggregate was determined by sieve analysis as shown in Fig. 1.

A polycarboxylate-based superplasticizer (MasterGlenium ACE 430) was used in this study to aid the dispersion of the GNPs in water and to achieve the desired workability in the cementitious matrix. This decision was based on previous research [47] indicating that polycarboxylate ether (PCE) superplasticizers effectively disperse carbon-based nanomaterials throughout concrete matrix. The concentration of GNPs = 0.133 g (0.025 % of the cement weight) was chosen in the current investigation, as it has shown excellent performance in achieving homogeneous dispersion and significantly improved the mechanical properties of cement-based composites in previous investigations [48]. GNPs used in this study were purchased from Cheap Tubes Inc., USA. Two different types of fibres were utilized: mono-filament polyvinyl alcohol fibre (PVA RECS 100) and polyolefin fibre (Polyex Mesh 2000). The microscopic images of GNPs, PO and PVA fibres are presented in Fig. 2, and their detailed characteristics are given in Tables 1 and 2, respectively.

A total of four different concrete mixture groups, labelled as A, B, C, and D, were designed to investigate the synergistic effects of GNPs combined with single and hybrid fibre reinforcement PO-PVA at varying dosages (0.1 %, 0.3 %, and 0.6 % to the total volume of concrete), according to mix proportion given in shown in Table 3. The first two mixtures were prepared as reference specimens where no fibre was used: plain concrete (R1) and plain GNPs-concrete (R2). In Groups A and B, the PO and PVA fibres were incorporated at a volume fraction of 0.1 %, 0.3 and 0.6 %, respectively. Group C used PO-PVA hybrid fibres with total volume fractions of: 0.2 % (0.1 % PO+0.1 % PVA), 0.6 % (0.3 % PO+0.3 % PVA), and 1.2 % (0.6 % PO+0.6 % PVA), and group D used PO-PVA hybrid fibres with total volume fractions of 0.4 % (0.1 % PO+0.3 % PVA), 0.4 % (0.3 % PO+0.1 % PVA), and 0.9 % (0.6 % PO+0.3 % PVA).

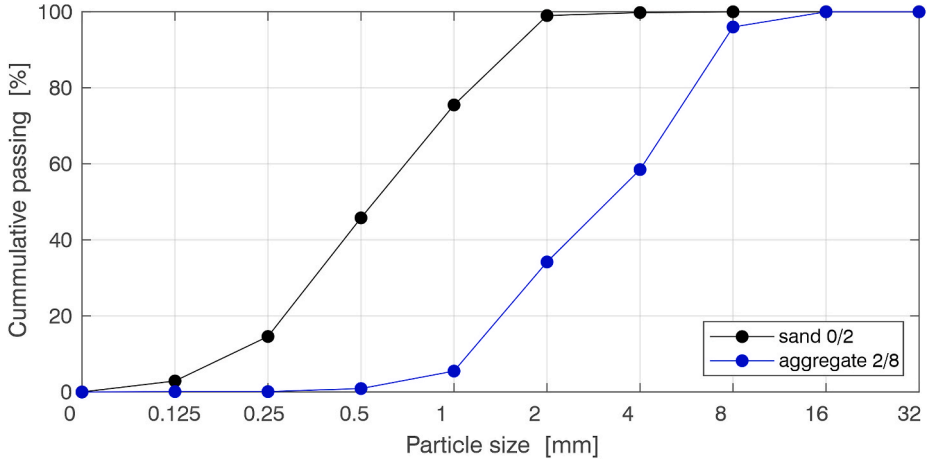

Fig. 1. Gradation curve of aggregates.

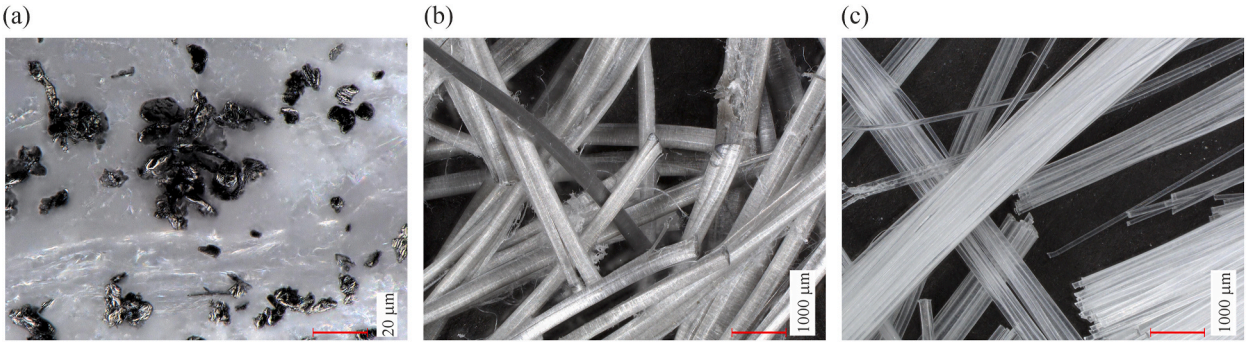

Fig. 2. Microscopic images of materials reinforcing concrete: (a) graphene nanoplatelets; (b) polyolefin fibres; and (c) polyvinyl alcohol fibres.

Table 1
Physical properties of GNPs (as supplied by manufacturer).

Specific Surface Area (m^2/g)	Average thickness (nm)	Diameter (µm)	Carbon content (%)	Elastic Modulus (GPa)	Tensile Strength (GPa)
500–700	8–15	>2	>97	1000	5

Table 2
Physical and mechanical properties of PO and PVA fibre (as supplied by manufacturer).

	Length (mm)	Equivalent diameter (mm)	Density (g/cm3)	Tensile strength (MPa)	Elastic modulus (GPa)
PO	24	0.02	0.91	550–650	>3
PVA	13	0.1	1.3–1.4	1200–1600	27–40

Table 3
Mix proportions.

Materials	Mixture ID	PCE (g)	GNPs (g)	PO (g)	PVA (g)
plain concrete	R1	0.133	0	0	0
plain concrete + GNPs	R2	0.133	0.133	0	0
Group A (GNPs + PO fibre)					
0.025%GNPs+0.1 % PO	A1	0.133	0.133	1.274	0
0.025%GNPs+0.3 % PO	A2	0.133	0.133	3.822	0
0.025%GNPs+0.6 % PO	A3	0.133	0.133	7.644	0
Group B (GNPs + PVA fibre)					
0.025%GNPs+0.1 % PVA	B1	0.133	0.133	0	1.82
0.025%GNPs+0.3 % PVA	B2	0.133	0.133	0	5.46
0.025%GNPs+0.6 % PVA	B3	0.133	0.133	0	10.92
Group C (GNPs + hybrid PO-PVA with the same dosages)					
0.025%GNPs+0.1 % PO+0.1 % PVA	C1	0.133	0.133	1.274	1.82
0.025%GNPs+0.3 % PO+0.3 % PVA	C2	0.133	0.133	3.822	5.46
0.025%GNPs+0.6 % PO+0.6 % PVA	C3	0.133	0.133	7.644	10.92
Group D (GNPs + hybrid PO-PVA with varied dosages)					
0.025%GNPs+0.1 % PO+0.3 % PVA	D1	0.133	0.133	1.274	5.46
0.025%GNPs+0.3 % PO+0.1 % PVA	D2	0.133	0.133	3.822	1.82
0.025%GNPs+0.6 % PO+0.3 % PVA	D3	0.133	0.133	7.644	5.46

3.2. Sample preparation

Ultrasonication is required to ensure uniform dispersion of GNPs in water, a common preparation method for graphene-reinforced cementitious composites. In this study, an ultrasonic processor (model UP400St), was used. First, the desired amount of water, GNPs and superplasticizer (PCE) were measured using an MA 210.R.NS balance. Water was then added, and the mixture was sonicated in the ultrasonic processor for 30 min with the following parameters: amplitude at 80 % and pulse at 70 %, with the power automatically adjusted. To cool the GNPs suspension during sonication, ice cubes were placed under the beaker. Meanwhile, all the dry materials (cement, sand, aggregate and fibres) were mixed in a Hobart mixer for 1 min at medium-low 80 rpm. After mixing, the sonicated GNPs

dispersion was added to the dry ingredients, and the mixing process continued for 3 min at medium-high 150 rpm. After mixing, the concrete mixture was placed into steel moulds and vibrated for densification after each casting. Sets of three 160 × 40 × 40 mm^3 prismatic specimens and sets of three 50 × 50 × 50 mm^3 cubic specimens were cast from each mix batch. According to EN 14889-Part, 2 standards the selected 160 × 40 × 40 mm^3 prismatic specimens are appropriate for a fibre length of PO 24 mm, as they provide a balance between achieving effective reinforcement and workability while adhering to recommended practices for fibre/specimen size ratios. All the specimens were stored at room temperature for 24 h under a sealed plastic bag to prevent water evaporation. After demoulding, the specimens were cured in a water tank with 95 ± 5 % relative humidity for 28 days prior to testing. A schematic diagram of the sample preparation process is shown in Fig. 3.

3.3. Testing setup and procedure

The compressive strength test was carried out using a CONT 50-C9032 machine, equipped with a load cell with a maximum capacity of 300 kN. Fig. 4 illustrates the test setup and a sample during testing. For AE analysis the selected prismatic specimens were subjected to the three-point bending test. The experimental setup for the three-point bending test is shown in Fig. 5(a). The tests were carried out using the Zwick/Roell Z10 Universal Testing Machine (UTM) equipped with a 10 kN load cell. Two steel supports were placed 120 mm apart, and the load was applied by a steel punch located at the centre of the tested beam. The specimens were first subjected to an initial load of 100 N and then loaded at a rate of 0.1 mm/min. During the bending procedure, the fracture process was monitored and characterized using an acoustic emission technique. AE signals were recorded using two VS45-H piezoelectric AE sensors (placement shown in Fig. 5(b). MAG4H magnetic holders are used to mount the AE sensor on the front of the specimen to ensure proper coupling and accurate detection of AE signals. In addition, a thin layer of silicone grease was applied between the sensors and the concrete surface. This configuration reduces signal attenuation and provides reliable data acquisition. Data acquisition was performed using the AMSY-6 system (Vallen Systeme GmbH) with a sampling rate of 5 MHz. The signal separation threshold was set at 42 dB.

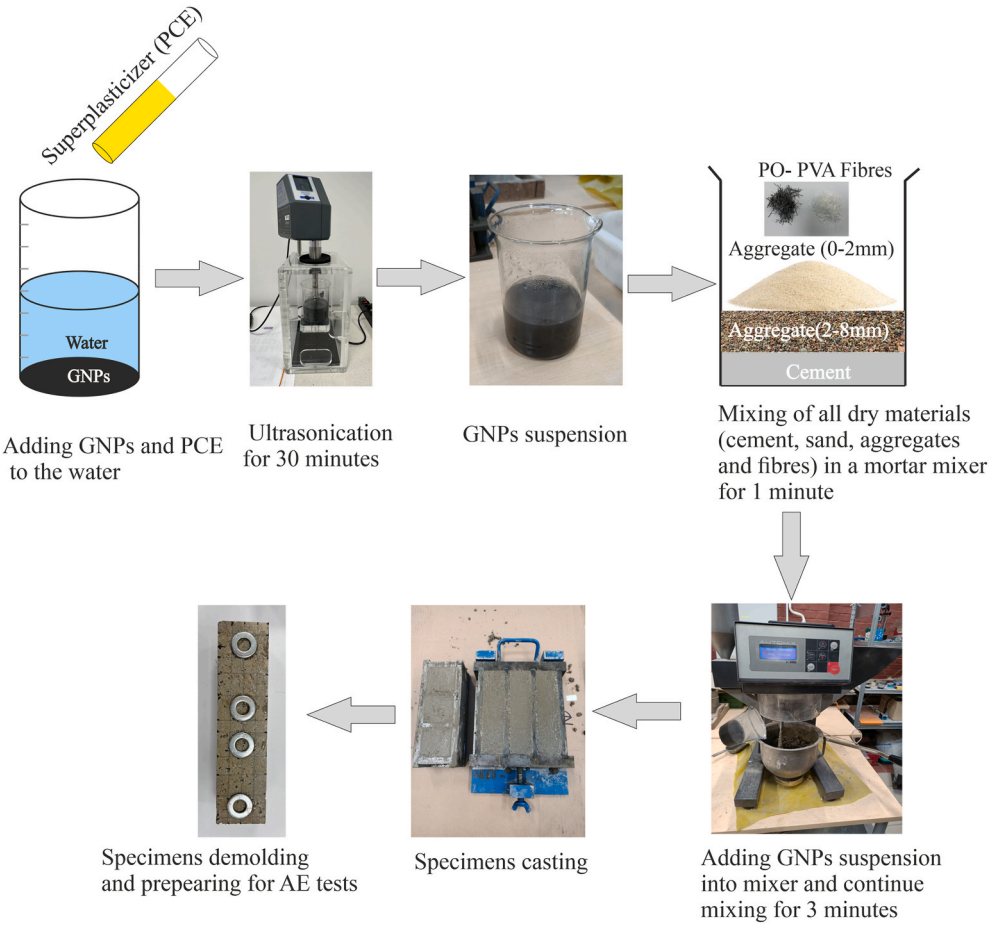

Fig. 3. Schematic diagram of the sample preparation process.

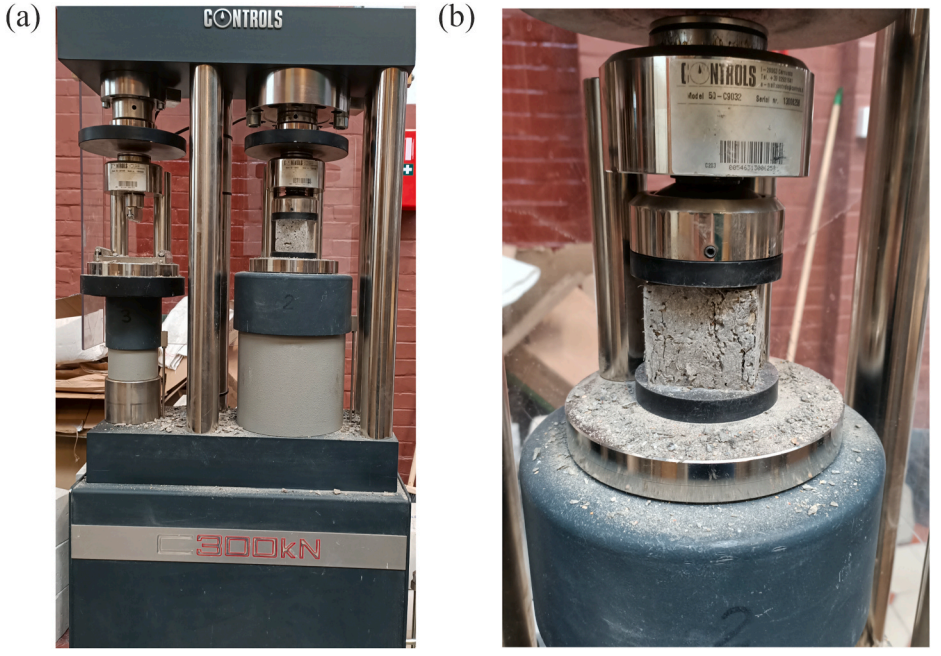

Fig. 4. Compressive strength test machine (a) and specimen inside the testing machine (b).

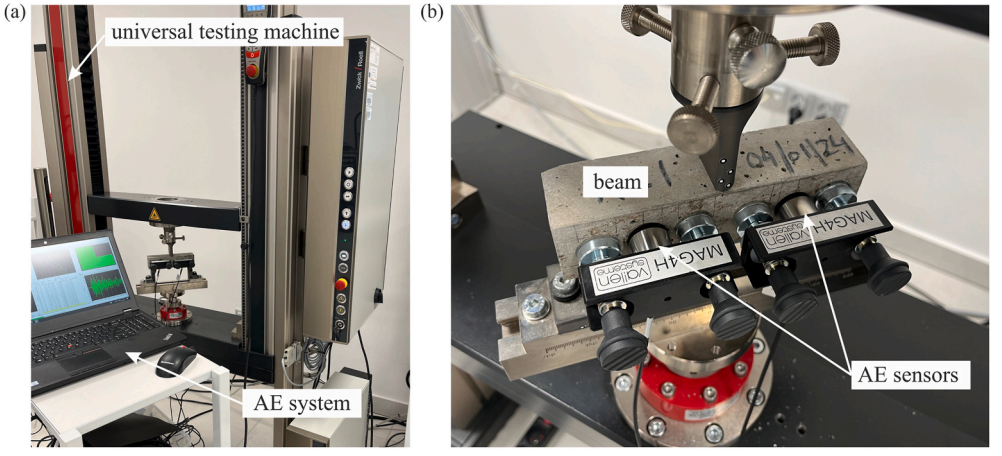

Fig. 5. Experimental setup for 3-point bending test (a) and specimen with the location of AE sensors (b).

3.4. Acoustic emission

Acoustic emission is a powerful NDT technique for monitoring damage evolution during mechanical testing. It can be demonstrated as a phenomenon in which a transient elastic wave is generated by the rapid release of energy within materials [49,50]. AE sensors attached to the surface of the samples detect these elastic waves and convert them into electrical signals so that they can be recorded. These signals can be analysed in real-time to provide valuable information on the evolution of damage. In this section, the AE analysis methods such as cumulative AE hits activity, spectral peak frequency distribution, cumulative AE energy, Ib-value analysis, signal intensity analysis, and RA-AF correlation were utilized to examine the fracture evolution induced by external bending load.

3.4.1. Ib-value method

The Ib-value approach, consistent with the improved b value, is obtained by adding statistical parameters from the amplitude distribution of AE events. The Ib-value can be calculated by using the following relation [51]:

$$Ib = \frac{\log_{10} N(\mu - \alpha_1\sigma) - \log_{10} N(\mu + \alpha_2\sigma)}{(\alpha_1 + \alpha_2)\sigma} \quad (1)$$

where $N(\mu-\alpha_1\sigma)$ denotes the accumulated number of AE event counts in which the amplitude is greater than $\mu-\alpha_1\sigma$; $N(\mu+\alpha_2\sigma)$ denotes the accumulated number of AE event counts where the amplitude is more than $\mu+\alpha_2\sigma$; μ and σ denotes the mean amplitude and standard deviation of amplitude distribution, respectively. Parameters α_1 and α_2 denote the user-defined constants depending on the amplitude distribution of AE events.

3.4.2. AE signal intensity

Intensity analysis evaluates the overall structural integrity and damage status of the structure, by calculating two parametric values based on AE signal strength: Historic Index (HI) and log severity $\left(\log_{10}S_r\right)$ [46]. HI index is calculated by analyzing the change in the slope of the cumulative signal strength over time of the most recent hits to the overall signal strength recorded for that specific channel [52], which can be computed as follows

$$HI(t)=\frac{N}{N-K}\frac{\sum_{i=K+1}^{N}S_{oi}}{\sum_{i=1}^{N}S_{oi}} \tag{2}$$

where $HI(t)$ refers the historic index at a given time t; N denotes the total number of AE hits recorded up to time t; S_{oi} represents the signal strength of ith hit and K is the empirical parameter constant that depends that varies on the number of AE hits and material type.

Parameter S_r represents the average of empirically derived constants based on the material type, which signifies the largest signal strength emission [52]. The $S_r(t)$ can be calculated using the formula:

$$S_r(t)=\frac{1}{J}\sum_{i=1}^{J}S_{oi} \tag{3}$$

where S_{oi} represents the signal strength of ith hit and J denotes the empirically derived constant related to material type.

The specific values for J and K values for concrete structures are provided in Table 4.

4. Results and discussion

4.1. Flexural and compressive strengths

The flexural strength and compressive strength, along with the standard deviation and coefficient of variation derived from all the prismatic specimens are presented in Tables 5 and 6, respectively. The results indicate that the incorporation of graphene into single and hybrid PO-PVA fibres could increase flexural strength depending on the fibre hybridization ratio (see Fig. 6(a)). However, its effect on compressive strength improvement is minimal and varied inconsistently, as shown in Fig. 6(b). Plain concrete specimen R1 served as a baseline, exhibiting flexural strength and compressive strength values of 8.38 MPa and 68.82 MPa, respectively. With the addition of GNPs at 0.025 wt% (R2), the value of flexural strength increased up to 10.25 MPa, whereas the compressive strength exhibited a slight improvement up to 70.32 MPa. Group A mixtures demonstrate that adding PO fibres at fibre contents of 0.1 vol%, 0.3 vol%, and 0.6 vol%, increased flexural strength values of 8.50 MPa, 9.39 MPa, and 9.09 MPa, while compressive strength values showed a marginal rise of 56.99 MPa, 71.48 MPa, and 70.70 MPa. For Group B mixtures, the addition of PVA fibres at the total fibre contents of 0.1 vol%, 0.3 vol%, and 0.6 vol%, yielded flexural strengths values of 8.84 MPa, 9.19 MPa, and 9.10 MPa, while the compressive strength varied inconsistently with values of 65.60 MPa, 72.43 MPa, and 65.74 MPa. When GNPs were combined with PO-PVA hybrid fibre reinforcement at total volume fractions of 0.2 % (0.1 % PO+0.1 % PVA), 0.6 % (0.3 % PO+0.3 % PVA), and 1.2 % (0.6 % PO+0.6 % PVA), flexural strength remained comparable to single-fibre systems with corresponding values of 9.01 MPa, 8.67 MPa, and 8.52 MPa; however, compressive strength exhibited a decreasing trend at higher fibre fractions with values of 72.42 MPa, 67.97 MPa and 54.10 MPa, respectively. Similarly for Group D mixtures, the compressive strength results further highlighted this inconsistency with values of 72.58 MPa, 71.27 MPa and 55.76 MPa, while flexural strength values were: 9.09 MPa, 7.85 MPa, and 8.68 MPa when total volume fractions of 0.4 % (0.1 % PO+0.3 % PVA), 0.4 % (0.3 % PO+0.1 % PVA), and 0.9 % (0.6 % PO+0.3 % PVA) of hybrid fibres combined with GNPs.

Notably, the Groups C and D mixtures demonstrated higher consistency in flexural performance with a lower COV value, suggesting that combining GNPs with hybrid PO-PVA fibres enhances reliability despite the lack of significant compressive strength improvements. The flexural and compressive results are summarised in Fig. 6 in the form of bar charts.

Table 4
K and J parameter values [42].

No. of hits (N)	≤50	51–200	201–500	≥501
K	Not applicable	N−30	0.85N	N−75
J		50		

Table 5
Results of bending tests for all samples.

Mixtures	Specimen ID			Flexural strength (MPa)			Mean value	Standard deviation (MPa)	COV (%)
R1	R1.1	R1.2	R1.3	7.78	8.19	9.16	8.38	0.71	8.45
R2	R2.1	R2.2	R2.3	9.72	9.70	11.34	10.25	0.94	9.19
A1	A1.1	A1.2	A1.3	8.61	7.89	8.99	8.50	0.56	6.56
A2	A2.1	A2.2	A2.3	9.03	8.83	10.32	9.39	0.81	8.62
A3	A3.1	A3.2	A3.3	8.64	8.15	10.48	9.09	1.23	13.51
B1	B1.1	B1.2	B1.3	9.02	9.38	8.13	8.84	0.64	7.28
B2	B2.1	B2.2	B2.3	9.79	8.47	9.31	9.19	0.67	7.26
B3	B3.1	B3.2	B3.3	9.73	9.47	8.12	9.10	0.86	9.49
C1	C1.1	C1.2	C1.3	9.02	9.03	8.97	9.01	0.03	0.34
C2	C2.1	C2.2	C2.3	8.44	9.09	8.48	8.67	0.36	4.18
C3	C3.1	C3.2	C3.3	8.68	8.96	7.93	8.52	0.53	6.21
D1	D1.1	D1.2	D1.3	9.25	8.49	9.52	9.09	0.53	5.87
D2	D2.1	D2.2	D2.3	7.91	7.51	8.14	7.85	0.32	4.04
D3	D3.1	D3.2	D3.3	8.24	8.81	8.98	8.68	0.38	4.42

Table 6
Results of compression tests for all samples.

Mixtures	Specimen ID			Compressive strength (MPa)			Mean value (MPa)	Standard deviation (MPa)	COV (%)
R1	R1.1	R1.2	R1.3	72.26	61.58	72.64	68.83	6.28	9.12
R2	R2.1	R2.2	R2.3	67.94	68.18	74.84	70.32	3.91	5.57
A1	A1.1	A1.2	A1.3	54.28	52.00	64.68	56.99	6.76	11.86
A2	A2.1	A2.2	A2.3	70.72	74.14	69.58	71.48	2.37	3.31
A3	A3.1	A3.2	A3.3	70.15	69.09	72.87	70.70	1.95	2.76
B1	B1.1	B1.2	B1.3	66.69	66.02	64.09	65.60	1.35	2.06
B2	B2.1	B2.2	B2.3	73.01	69.42	74.85	72.43	2.76	3.81
B3	B3.1	B3.2	B3.3	70.82	63.78	62.61	65.74	4.44	6.75
C1	C1.1	C1.2	C1.3	74.97	69.43	72.86	72.42	2.79	3.86
C2	C2.1	C2.2	C2.3	70.87	64.35	68.69	67.97	3.32	4.88
C3	C3.1	C3.2	C3.3	47.33	61.29	53.68	54.10	6.99	12.92
D1	D1.1	D1.2	D1.3	75.00	72.06	70.68	72.58	2.21	3.04
D2	D2.1	D2.2	D2.3	69.74	71.00	73.07	71.27	1.68	2.36
D3	D3.1	D3.2	D3.3	58.41	45.06	63.81	55.76	9.65	17.31

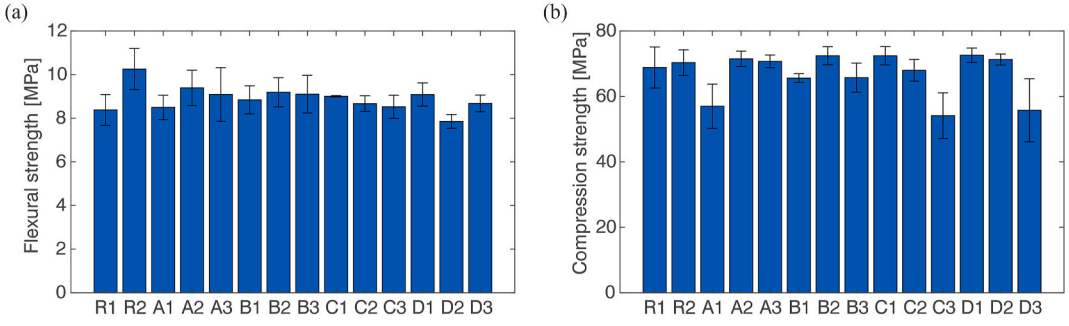

Fig. 6. Flexural strength (a) and compression strength (b) of all the tested specimens.

4.2. Load-deflection curves

Only one beam from each group was selected for further AE analysis, as results were consistent between samples. The load-deflection graphs for the selected specimens are presented in Fig. 7. The results show that all tested specimens displayed a similar linear trend in the pre-peak region of their load-deflection curves. After reaching the maximum flexural strength the curves were dropped sharply. The peak load values recorded for the specimens were 3257.57 N and 3447.49 N for the reference beams (R1 and R2), 3196.56 N, 3669.33 N, and 3726.09 N for group A beams (A1, A2 and A3), 2890.11 N, 3308.65 N, and 2886.43 N for group B beams (B1, B2 and B3), 3211.17 N, 3230.68 N, and 3184.37 N for group C beams (C1, C2 and C3), and 3384.89 N, 2893.68 N and 3191.31 N for group D beams (D1, D2 and D3).

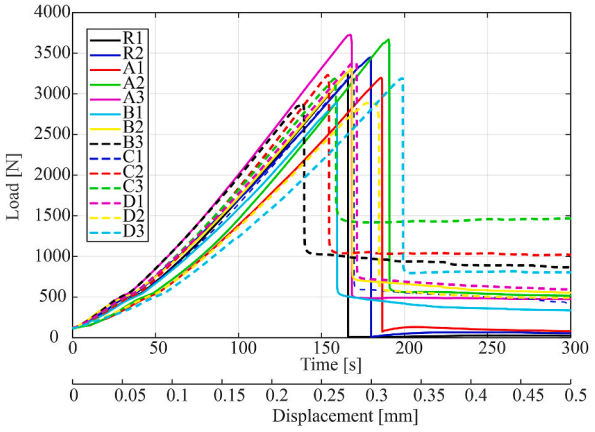

Fig. 7. Load-deflection and load-time curves of selected specimens.

4.3. AE results analysis

4.3.1. Cumulative hits and spectral peak frequency analysis

Cumulative hit analysis identifies the extent of microcracking activity within the fractured concrete and corresponds to its mechanical performance characteristics. The increasing trend in the slope of the cumulative hits curve indicates more active AE signals and an increased number of microcracks generation as well as propagation within the microstructure of concrete [50]. On the other hand, the spectral peak frequency analysis is an important parameter of the AE signal that provides valuable insight related to the failure mechanisms, crack propagation dynamics, and energy dissipation processes that occurred during fracturing [46]. Previous studies have suggested that distinct frequency ranges within the AE signal spectrum can be correlated with specific failure modes in fibre-reinforced concrete [43]. For instance, AE signals ranging between 100 kHz and 150 kHz are often attributed to matrix microcracking, while frequencies between 150 kHz and 250 kHz are commonly associated with fibre/matrix debonding. Similarly, frequencies in the range of 350–500 kHz are associated with fibre rupture or pull-out events [53]. Thus, the combined application of cumulative AE hits activity and spectral peak frequency distribution is essential to characterize the overall fracture mechanism of fibre-reinforced concrete.

The correlation between the cumulative AE hits activity and the spectral peak frequency distribution of the plain concrete specimen (R1) and the plain GNPs-specimen (R2) is depicted in Fig. 8(a and b). The plain concrete specimen (R1) exhibited a single dominant spectral peak frequency band in the pre-peak region of 50–150 kHz, which may correspond to the cracking of the cementitious matrix based on prior studies [43,54]. At peak load, a significant increase in the cumulative AE hits curve was observed, with the peak frequency distribution occurring predominantly between 50 and 300 kHz, suggesting an abrupt matrix fracture event.

This indicates that in the absence of reinforcement, the failure of the plain specimen R1 was controlled only by tensile cracking, exhibiting an obvious brittleness nature. In contrast, the addition of GNPs, significantly affected the fracture characteristics of the plain specimens, as evidenced by changes in the spectral peak frequency patterns and the higher cumulative AE hit rate compared to the R1 specimen (see Fig. 8(b)). This effect occurs because the substitution of graphene nano-reinforcement elements can act as stress concentrators and nucleation sites for microcracks, leading to increased AE activity. The time-frequency plot for the R2 specimen exhibited two distinct frequency ranges in the pre-peak region: the lower frequency range of 50–150 kHz and the higher frequency range of 150 kHz–350 kHz, respectively. These dual peaks may correspond to two distinct failure mechanisms. The lower frequency range could be associated with matrix cracking, potentially influenced by the presence of graphene nanosheets, while the higher frequency range might reflect interfacial debonding between graphene and cementitious composites. Fig. 8(c–n) illustrates the combined trend of cumulative hit activity and spectral peak frequency distribution of AE signals for the selected specimens from the four mixture groups (A, B, C, and D). For Group A specimens, the relationship between cumulative AE hit activity and the spectral peak frequency distribution of GNPs reinforcing with total PO fibre contents of 0.1 vol%, 0.3 vol%, and 0.6 vol % are presented in Fig. 8 (c–e). The results suggest that the inclusion of GNPs with different PO fibre volume fractions considerably increased the cumulative AE hits activity and exhibited a distinct spectral frequency band in both the pre-peak and post-peak phases. For A1 and A2 specimens, higher-frequency emissions (50–300 kHz) of AE signals and the upward trend in the cumulative hits curve were observed during initial loading events. This increase may be related to the smoother surface morphology of PO fibres, which could influence interfacial bonding with the wrinkled GNPs. Consequently, this likely resulted in pronounced microstructural changes and increased microcracking activity at the start of the fracture process.

An increase in PO fibre dosage to 0.6 % (A3 specimen) resulted in improved initial crack resistance (fibre-bridging stress) within the PO-GNPs matrix during the pre-peak phases of fracture, along with a linear cumulative hits curve compared to A1 and A2 beams. In the post-peak phases, a continuous rise in the cumulative AE hits activity was observed, along with the higher frequency distribution. This increase is attributed to the fibre ruptures leading to the propagation and development of macrocracks. The maximum cumulative hit values recorded were 6493 for the A1 specimen, 10360 for the A2 specimen, and 8720 for the A3 specimen, which further supported

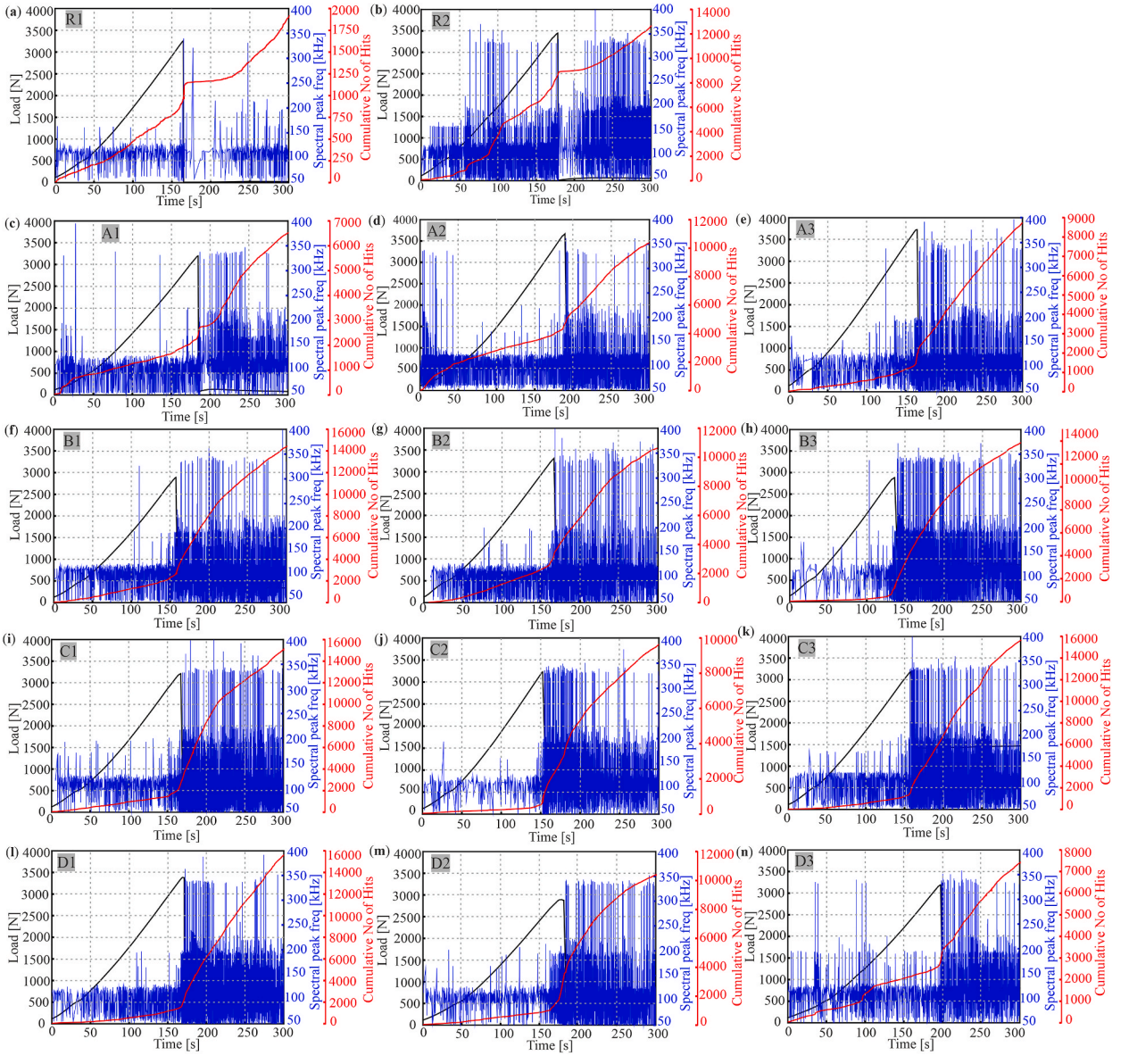

Fig. 8. The combined trend in cumulative AE hits activity and spectral peak frequency distribution of tested specimens alongside load-time curves: (a) R1; (b) R2; (c) A1; (d) A2; (e) A3; (f) B1; (g) B2; (h) B3; (i) C1; (j) C2; (k) C3; (l) D1; (m) D2; (n) D3.

this observation. For Group B specimens, the combined trend of cumulative hits activity and spectral peak frequency distribution of AE signals influenced by the addition of GNPs with total PVA fibre contents of 0.1 vol%, 0.3 vol%, and 0.6 vol % is depicted in Fig. 8(f–h). The results indicate that B1 and B2 specimens exhibited a prevalence of lower frequency spectra (50–150 kHz) during the pre-peak fracture phase, accompanied by a steady increase in the accumulated AE hits curve. This, compared to the A1 and A2 specimens, implies that PVA fibres with their tangled structure and abundant surface hydroxyl groups, promote superior hydrogen bonding with GNPs within the matrix. Consequently, a more robust interfacial bond was formed between the PVA-GNPs matrix, enabling efficient stress transfer and more effective bridging of the cracks compared to the PO-GNPs specimens. In the post-peak phase, the PVA-GNP beams exhibited a higher cumulative AE hit rate and frequency of AE signals. This was attributed to being completely pulled out of the PVA fibres from the cracked bridged area. The maximum cumulative hit values observed were 14385 for the B1 specimen, 10595 for the B2 specimen, and 13800 for the B3 specimen indicating a higher density of AE signals compared to the Group A specimens.

Fig. 8(i–k) illustrates the distribution of cumulative AE hits activity and spectral frequencies of AE signals for Group C specimens, reinforcing GNPs with hybrid PO-PVA fibre reinforcement at total volume fractions of 0.2 % (0.1 % PO+0.1 % PVA), 0.6 % (0.3 % PO+0.3 % PVA), and 1.2 % (0.6 % PO+0.6 % PVA). The results of the Group C specimens show that introducing GNPs to the hybrid fibre dosage may enhance the interfacial bonding between the fibres and the matrix, as inferred from the AE activity patterns.

However, microcrack propagation is initiated for the C1 specimen at the onset of the fracture process. This micro-cracking activity is reflected by the increasing trend of the cumulative hits curve and the concentration of peak frequencies within the range of (50–200 kHz) during the pre-peak phase, which could indicate fibre-matrix debonding. This observation suggests that the addition of a low volume fraction of 0.1 % PO and PVA fibres may lead to more dispersed hybrid fibres within the matrix, potentially resulting in weak interfacial bonding. This could create uneven stress distribution within the matrix, activating the initiation of microcracks. In the post-peak phase, this debonding behaviour intensifies, leading to fibre ruptures within the crack bridging zone and a subsequent increase in the frequency and cumulative AE hit rate. When the hybrid fibre content is set at total volume fractions of 0.6 % (0.3 % PO+0.3 % PVA), the C2 specimen exhibits a stable pattern of accumulated AE events and the dominance of lower frequency signals (50–150 kHz) during the pre-peak phase of fracture. This may indicate the beneficial reinforcing effects with GNPs, potentially due to improved crack bridging small cracks and energy absorption. However, when the hybrid fibre dosage is increased to 1.2 % (0.6 % PO+0.6 % PVA) in the C3 specimen, it produces a similar reinforcing effect with GNPs as observed in the C1 specimen. The maximum accumulated AE hit values recorded were 15085 for the C1 specimen, 9574 for the C2 specimen, and 15645 for the C3 specimen. These values reveal both C1 and C3 configurations exhibit higher microcracking activities compared to C2.

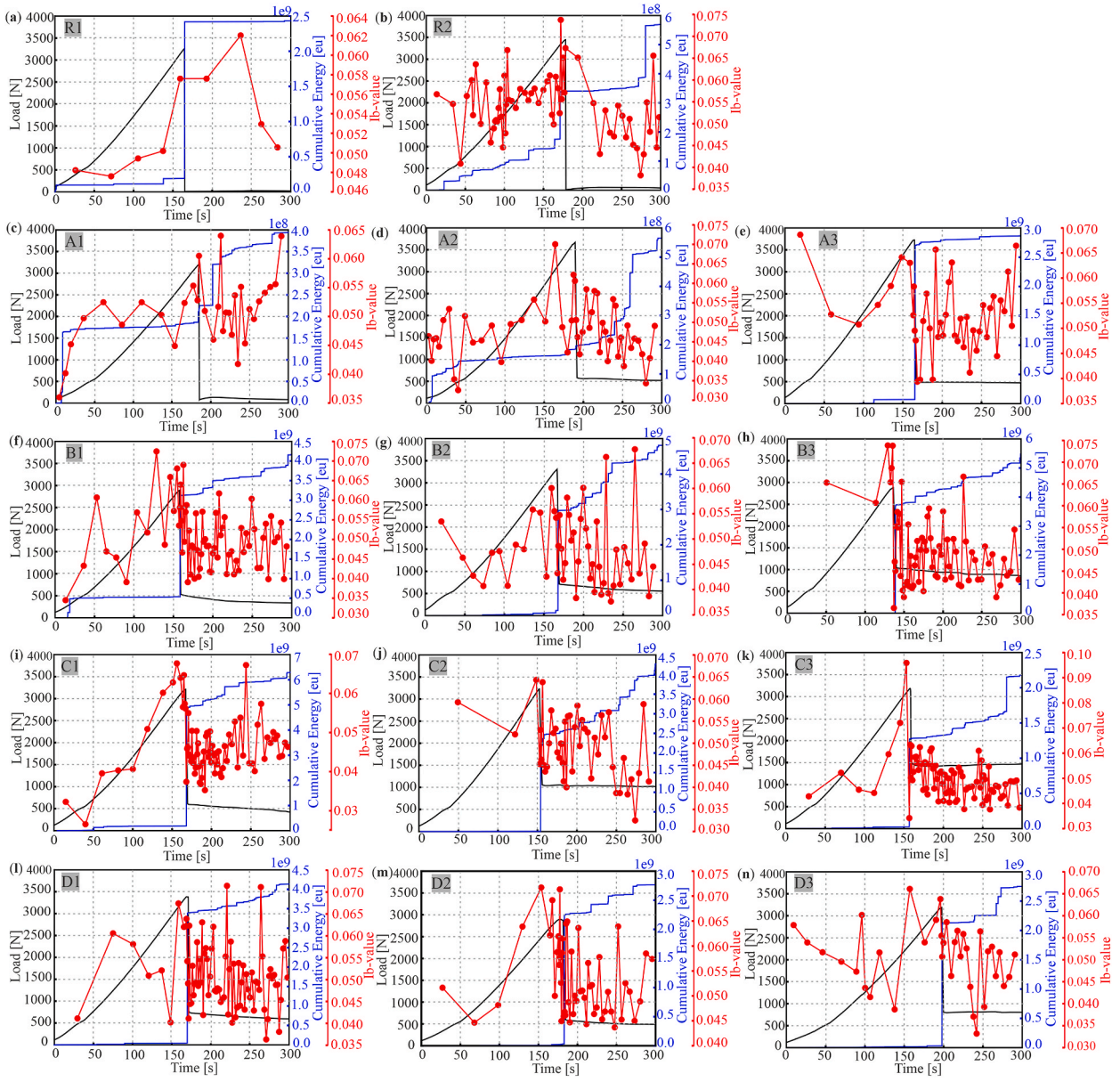

Fig. 9. The trend of cumulative AE energy and Ib-value analysis of tested specimens, alongside load-time curves: (a) R1; (b) R2; (c) A1; (d) A2; (e) A3; (f) B1; (g) B2; (h) B3; (i) C1; (j) C2; (k) C3; (l) D1; (m) D2; (n) D3.

The effect of incorporating GNPs into a hybrid fibre matrix containing total volume fractions of 0.4 % (0.1 % PO+0.3 % PVA), 0.4 % (0.3 % PO+0.1 % PVA), and 0.9 % (0.6 % PO+0.3 % PVA) for Group D specimens, is presented in Fig. 8(l–n). In the D1 specimen, with a lower PO fibre content (0.1 %) and a higher PVA fibre content (0.3 %), the addition of GNPs may have enhanced the interfacial bond strength between GNPs and the surrounding matrix (PO-PVA/GNPs) during the pre-peak region. This is inferred from the stable cumulative hits curve and a lower frequency distribution (50–150 kHz) of AE signals. This means that the microvoids of the hybrid PO-PVA/matrix were filled with graphene nano-reinforcement, which effectively strengthened the matrix and hindered the initiation and propagation of microcracks. Similarly, by increasing the PO fibre content to 0.3 % and reducing the PVA fibre content to 0.1 % (specimen D2), comparable reinforcement effects with GNPs were achieved, as observed in the D1 specimen. In this case, the frequency of AE signals was concentrated between (50–200 kHz) and a gradual increase in cumulative AE hits was detected, indicating a beneficial reinforcement effect during the initial fracturing process. However, by further increasing the PO content to 0.6 % while keeping the PVA content constant at 0.3 % (specimen D3), a higher frequency emission of AE events (>250 kHz) and an upward trend in the cumulative hits curve was observed, indicating abrupt microcracking activity during the initial damage phase. This may be due to the higher dosage of PO fibres compared to PVA, which could increase the likelihood of fibre agglomeration effect due to their hydrophobic nature. Such agglomeration might weaken the interfacial interaction with GNPs, potentially causing debonding between the fibres and the cementitious matrix. The maximum cumulative hit values monitored were 15672 for the D1 specimen, 10385 for the D2 specimen, and 7373 for the D3 specimen. These values indicate that the D1 configuration exhibited significantly has the highest microcracking activity, among the three specimens.

4.3.2. Cumulative AE energy and Ib-value analysis

This section provides the synergistic effects of GNPs combined with single and hybrid fibre reinforcement on crack propagation and damage mechanisms for Groups A, B, C, and D specimens, as illustrated by cumulative AE (C-AE) energy and Ib-value trends. The AE energy served as a characteristic parameter of the AE signal, calculated by the mean area under the AE envelope during any event. The cumulative AE energy correlates with the extent of damage and the sudden increase in the slope of cumulative energy signifies damage initiation and progression in RC structures [55]. The cumulative AE (C-AE) energy trends and Ib-values for the plain concrete specimen (R1) and plain GNPs-reinforced specimen (R2), along with the load-time curve are depicted in Fig. 9(a and b). In the R1 specimen, the C-AE energy curve initially increased before levelling off at the maximum load, coinciding with a decrease in the Ib-value. At peak load, an abrupt increase in C-AE energy occurred, indicating an abrupt matrix fracture event. This suggests that in the absence of reinforcement in plain concrete, the failure in the R1 specimen was primarily controlled by the propagation of tensile cracks, demonstrating a brittle nature. In contrast, the R2 specimen exhibited a distinct pattern throughout the fracturing phase. During the pre-peak loading, the C-AE curve showed a stepwise increment, while the Ib-value fluctuated. This may indicate that well-dispersed GNPs enhance the interfacial bonding between the cement matrices, potentially resulting in a denser and stronger matrix. Such a stronger matrix could better resist crack initiation and propagation. As a result, the GNPs-reinforced beam demonstrated improved energy dissipation and deformation resistance during the fracture process compared to the R1 specimen.

For Group A specimens the synergistic effect of GNPs with total volume fractions of PO fibre contents at 0.1 %, 0.3 %, and 0.6 % on the relationship between C-AE energy and Ib-value analysis is shown in Fig. 9(c–e). In the A1 and A2 specimens, a decrease in the Ib-value alongside a sudden increase in C-AE energy was observed during the initial loading events, indicating frequent micro-crack expansion. As the load gradually increased, the Ib-value curve exhibited fluctuations, which may present a change in the size of the cracks and propagation. These fluctuations in Ib-value could be attributed to the bridging effect of the fibres on the cracks. At the same time, the C-AE energy gradually increased until reaching the peak load, suggesting the expansion and eventually merging of multiple microcracks expanded to form visible cracks. After the primary fracture event, the Ib-value sharply decreased to the minimum, indicating the occurrence of macro-cracks within the specimen. Notably, specimen A3 displayed a distinct behaviour during the pre-peak loading stage, characterized by a stable C-AE curve and a progressively increasing Ib-value trend. This may indicate that by increasing PO fibre content to 0.6 % the interfacial adhesion between PO fibres and GNPs was significantly enhanced during the pre-peak loading events. At a peak-loading stage, the C-AE energy spiked to higher values, coinciding with a reduced Ib-value (0.039) compared to specimens A1 and A2 (0.045 and 0.042, respectively). This indicates that the A3 specimen experienced larger-scale fractures during the primary cracking stage due to the increased fibre content. After the peak-loading stage, the C-AE profile remained flat, representing the residual cracking stage with the highest AE energy compared to specimens A1 and A2.

Fig. 9(f–h) illustrates the distribution characteristics between C-AE energy and Ib-value of synergistic effects of GNPs with total PVA fibre contents of 0.1 vol%, 0.3 vol%, and 0.6 vol % for Group B specimens. The behaviour of the PVA-GNPs specimens differed significantly from that of the PO-GNPs specimens, as evidenced by the variations in C-AE values and Ib-values. In the B1 specimen, minor microcrack expansion during initial loading events within the matrix may have led to an increase in the Ib-value, along with the spike of the C-AE profile. As the load progressed, fluctuations in the Ib-value trend occurred, which could be related to the expansion of microcracks within the matrix, while the C-AE profile remained stable. At peak strength, a sudden increase in C-AE energy and a sharp drop in Ib-value of 0.042 were observed, suggesting failure dominated by macroscopic crack propagation. Specimens B2 and B3, exhibited an increasing Ib-value profile during the pre-peak loading phase, accompanied by a stable C-AE energy profile. At peak strength, the minimum Ib-value for the B2 specimen was 0.046, while the B3 specimen exhibited the most significant drop of 0.036 Ib-value value. Following the main fracture event, the B3 specimen showed the highest emission of C-AE, indicating the occurrence of larger-scale macrocracks during the main cracking stage.

For Group C beams, the reinforcing effects of GNPs in a hybrid PO-PVA fibre matrix at total volume fractions of 0.2 % (0.1 % PO+0.1 % PVA), 0.6 % (0.3 % PO+0.3 % PVA), and 1.2 % (0.6 % PO+0.6 % PVA) on the distribution characteristics between C-AE energy and Ib-value are presented in Fig. 9(i–k). In the pre-peak fracturing phase, the C-AE profile for the C2 specimen remained stable,

while the Ib-value increased. This may indicate stronger interfacial between hybrid PO-PVA fibres and GNPs when equal dosages (0.3 %) of PO and PVA fibres were combined with GNPs. This configuration effectively arrested the crack growth mechanism within the matrix. As microcracks merged to form larger macrocracks, the GNPs acted as a micro-reinforcement, bridging the microvoids between the PO-PVA fibres and delaying the progression of macroscopic fractures. However, specimens C1 and C3 exhibited the lowest Ib-values (0.037 and 0.0342, respectively) during the main fracture event compared to the C2 specimen (0.046). These lower Ib-values suggest that the C2 configuration exhibited greater resistance to cracking and extended post-cracking behaviour. When the PO and PVA fibre content is increased to 1.2 % (0.6 % PO+0.6 % PVA) the reinforcing effect of GNPs is diminished, resulting in a decreasing Ib-value trend.

Fig. 9(l–n) shows the hybridization effect of PO-PVA fibres integrated with GNPs at total volume fractions of 0.4 % (0.1 % PO+0.3 % PVA), 0.4 % (0.3 % PO+0.1 % PVA), and 0.9 % (0.6 % PO+0.3 % PVA) for Group D specimens on the distribution characteristics between C-AE energy and Ib-value. During the initial fracture events, stable C-AE profiles and increasing Ib-values were observed in all three specimens, which may indicate enhanced resistance to early crack propagation. After the main cracking stage, the D1 specimen exhibited a step-wise increase in C-AE and greater fluctuation of Ib-value, suggesting a slower transition from microcrack propagation to macrocracks. This suggests strong reinforcing effects in the D1 specimen, demonstrating improved post-cracking fracture behaviour compared to the D2 and D3 specimens.

4.3.3. AE signal intensity analysis

Fig. 10 illustrates the varying degrees of damage over time in all the examined beam groups (A, B, C, and D) using AE signal intensity parameters; the Historical Index (*HI*), and the log severity index $\log_{10}(S_r)$. The *HI*(*t*) curves for all beam groups, except for the plain concrete beam (R1), displayed multiple local peak values, indicating discrete damage events in these composite materials during loading. Each local peak aligned with a sharp increase in the $\log_{10}S_r$ curve, indicating new damage formation within the specimen. The results also highlighted distinct peak *HI*(*t*) values across different beam mixture groups, implying that the integration of GNPs with PO and PVA fibres in various proportions significantly influenced the damage accumulation behaviour within the composite specimens.

The plain concrete (R1) specimen exhibited subpar performance under bending load, characterized by an abrupt failure with a single sharp peak in the *HI*(*t*) curve (*HI* = 6.0). This indicates the absence of additional reinforcement in plain specimens led to uncontrolled crack propagation, resulting in catastrophic failure. In contrast, the R2 specimen exhibited significantly higher fracture resistance, as indicated by its *HI*(*t*) curve, which showed a minimum peak of 4.47 at 170 s and a subsequent maximum peak of 5.71 at 280 s. These multiple peaks may suggest higher microcracking events and enhanced energy absorption capacity before ultimate

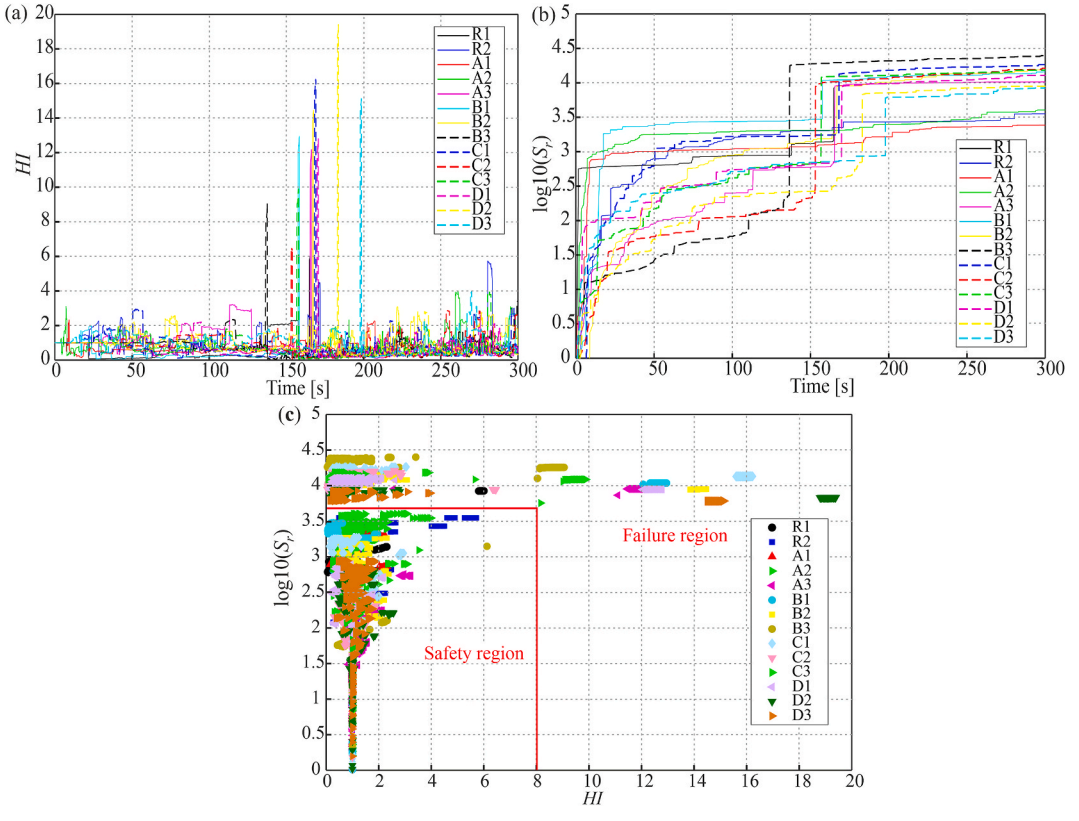

Fig. 10. The changing trend of HI and $log_{10}S_r$ values over time values for reference specimens and tested specimens from four different mix groups: (a) HI versus time; (b) $log_{10}S_r$ versus time; and (c) the relationship between HI and $log_{10}S_r$ plot.

failure. In Group A, specimens A1 and A2 exhibited a distinct fracture behaviour compared to the A3 specimen. The *HI*(*t*) curves for A1 and A2 showed multiple local peaks, indicating numerous microcracking events throughout the loading process. Conversely, the A3 specimen exhibited a single peak value of 12.1 at 166 s, suggesting a more sudden fracture. The peak values of 2.2 and 3.9 for the A1 and A2 specimens, occurred later at 209 and 259 s, respectively. These data suggest that the inclusion of GNPs in specimens with PO fibre contents between 0.1 % and 0.3 % (A1 and A2 specimens) enhanced the fibre-bridging effect with GNPs, potentially leading to a higher number of initial microcracks compared to the A3 specimen. However, these numerous microcracks may have contributed to enhanced post-cracking performance. When the PO fibre dosage increased to 0.6 % (A3 specimen), the resulting PO-GNPs matrix potentially enhanced the initial cracking stress. However, after initial crack formation, it may have led to the rapid development of

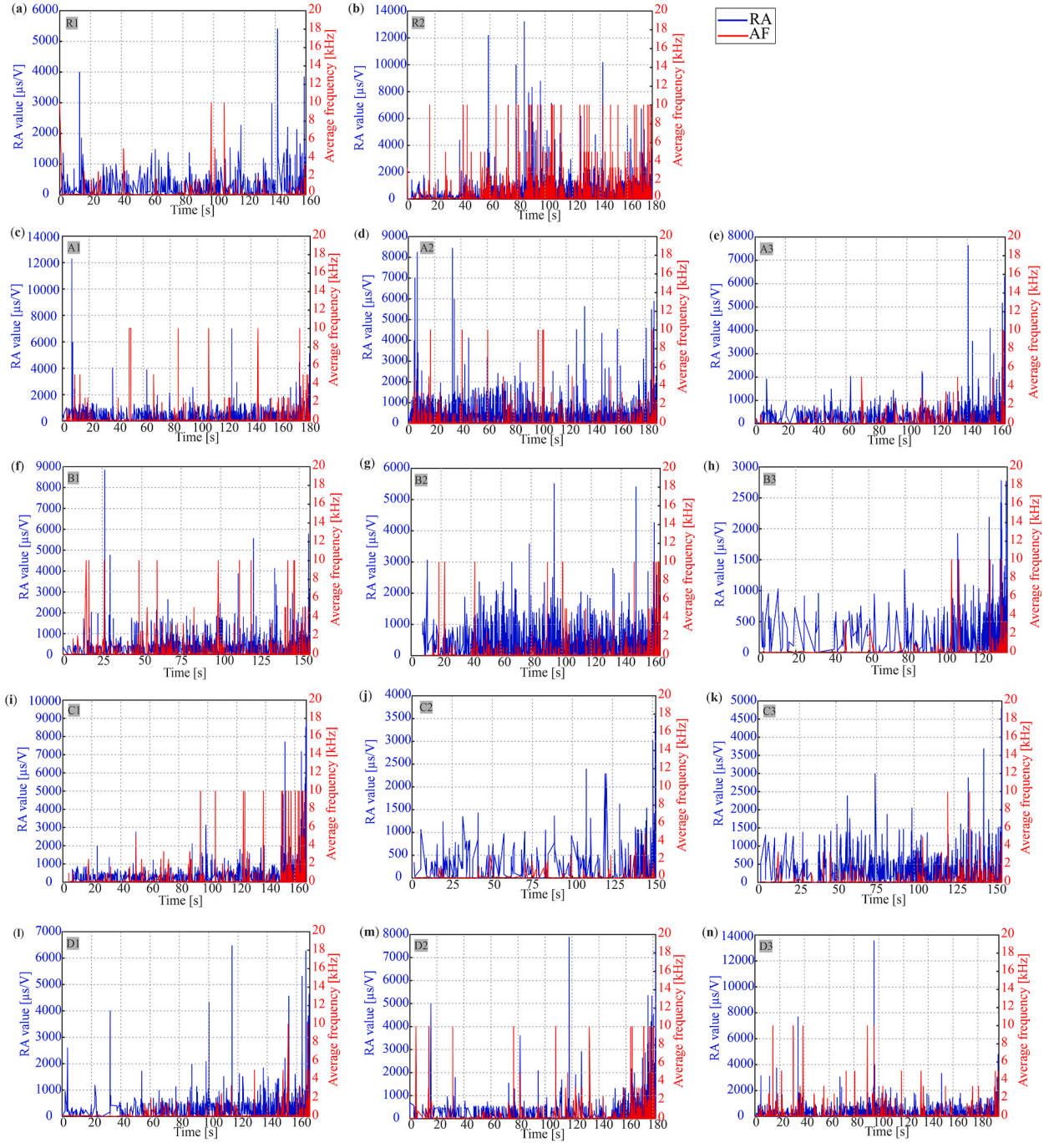

Fig. 11. Correlation AF-RA analysis of tested specimens: (a) R1; (b) R2; (c) A1; (d) A2; (e) A3; (f) B1; (g) B2; (h) B3; (i) C1; (j) C2; (k) C3; (l) D1; (m) D2; (n) D3.

larger-scale macro-cracks within the composite, reducing material post-fracture behaviour.

The *HI*(*t*) values for Group B specimens were significantly higher than those for Group A specimens, indicating a potential difference in their damage accumulation behaviour. Specimen B1 exhibited a maximum HI value of 12.9 at 158 s, indicating a multi-stage damage process, while specimen B3 had fewer peaks and a lower maximum value of 9.07 at 137 s. However, specimen B2 demonstrated a high number of peaks and a maximum *HI*(*t*) value recorded of 14.4 at 167 s. These results may suggest that incorporating GNPs with PVA fibre at volume fractions between 0.1 % and 0.3 % (B1 and B2 specimens) enhanced the bridging effects within the matrix, potentially leading to gradual energy release during main fracture events. This could indicate improved post-cracking behaviour, delaying the formation of new cracks after a major fracture event. The *HI*(*t*) curves for Group C specimens, showed continuous variation throughout the loading process, with consistently maintaining lower *HI*(*t*) values. Among the three specimens, the C2 specimen exhibited a lower maximum *HI*(*t*) value of 6.4 at 153 s compared to the C1 and C3 specimens (16.2 and 9.9 at 168 and 157 s, respectively). Group D specimens exhibited a distinct fracture behaviour with consistently higher *HI*(*t*) values fluctuating throughout the loading process, suggesting ongoing damage accumulation. The peak *HI*(*t*) values for Group D specimens were the highest of all groups, suggesting that the incorporation of the GNPs into a composite material containing a hybrid fibre matrix might have resulted in a complex damage mechanism. The presence of GNPs with varying PO-PVA content may have facilitated multiple bridging effects, potentially enhancing microcracking events and leading to extensive larger microcracks within the matrix. Following the peak loading stage, these microcracks likely continued to propagate and coalesce, worsening specimen damage. This is evidenced by significantly higher *HI*(*t*) values observed for the D2 and D3 specimens (19.4 at 183 s and 15.0 at 193 s, respectively), compared to the D1 specimen, which had a lower maximum peak value of 12.8 at 170 s.

Fig. 10(b) explores the severity level of the tested specimens using the rate of change of the slope line in the $\log_{10}S_r$ versus time plot. The analysis revealed this rate increased rapidly for all tested specimens during the initial fracturing stage, signifying high sensitivity of the $\log_{10}S_r$ values to microcrack initiation within the specimens. Whenever the *HI* value fluctuated over time, the $\log_{10}S_r$ value also showed a continuous increase, indicating a possible correlation between these two parameters. Specimens with higher values for both the $\log_{10}S_r$ and *HI*(*t*) indices were interpreted as an indication that the specimen was in a critical state with increased susceptibility for further damage; a sudden rise in the $\log_{10}S_r$ value could signal a high potential for further damage within the specimens. The analysis underscored the differences in damage severity among all tested specimen configurations; configuration B3 exhibited the highest damage index with the largest $\log_{10}S_r$ value of 4.3 and a sharp increase in curve rate change. However, configurations B2, C2, and D1 demonstrated optimal performance regarding severity level, with multiple knee values in their $\log_{10}S_r$ curves. These configurations displayed step-wise increments in slope value alongside multiple peaks, indicating a more controlled damage progression; multiple peaks suggested discrete damage events while step-wise increments reflected the material's ability to slow down crack propagation resulting in lower overall damage severity. A safe zone was established using a boundary line constructed from the correlation between *HI* and $\log_{10}S_r$ values at material failure points depicted in Fig. 10(c). The diagram presented a safer zone of ($HI = 8$ and $\log_{10}S_r = 3.7$), where the bottom left quadrant represented minimal damage while the upper right quadrant indicated more severe damage. Configurations A2, B2, C2, and D1 outperformed this safe zone threshold existing with a more robust and safer damage level compared to it. This finding aligned with earlier conclusions drawn from the cumulative AE hits and spectral peak frequency analysis as well as the cumulative AE energy and Ib-value analysis.

4.3.4. Classification of damage progression using RA and AF analysis

Rise angle (RA) and average frequency (AF) are crucial acoustic emission parameters for determining the mode of cracking in materials [56]. Signals with high RA and low AF values are typically associated with shear crack formation, whereas low RA and high AF values are indicative of tensile crack formation [42]. According to the previous observations, high AF values typically appear in the initial stages of beam flexural testing, suggesting the formation of tensile cracks. Conversely, the later stages are characterized by relatively higher relative RA amplitude values compared to AF, indicating the development of shear cracks [57,58].

The AF-RA correlation analysis of the reference specimens R1 and R2 is illustrated in Fig. 11. In the RA-AF analysis, all prismatic specimens were tested up to the peak loading stage to better understand the fracture mechanisms and damage evolution during the early stages of loading. As can be seen in Fig. 11(a and b), the R2 specimen exhibited higher AF and RA values compared to the R1 specimen throughout the fracture process. This suggests that the presence of GNPs may influence the crack propagation mechanism, potentially by acting as a bridging reinforcement within the matrix. Fig. 11(c–e) illustrates the time-dependent variations of AF and RA for Group A specimens, which integrate GNPs with different PO fibre contents. Specimen A1 demonstrated higher AF and lower RA values, indicating a higher proportion of tensile cracks and potentially more brittle fracture behaviour. This observation may be attributed to the emergence of a greater number of microcracks during the initial loading stage. As the PO fibre contents increased (in A2 and A3 specimens), AF values decreased while RA values increased (Fig.11(d) and (e)). This suggests a shift in the main fracture type to more widespread shear cracks over time, likely due to progressive microstructural changes such as fibre matrix de-bonding and pull-out activity under initial loading. This may have contributed to a higher overall severity of damage compared to the A1 specimen. Fig. 11(f–h) shows the cracking pattern in Group B specimens by analysing the variation of AF and RA values over time. Notably, the Group B specimens exhibited consistently higher RA values throughout the cracking process, with this trend intensified as the PVA fibre content increased. This indicates that the presence of GNPs alongside PVA fibres may have facilitated stronger interfacial bonding between the fibres and the surrounding matrix, potentially making it more difficult for tensile cracks to initiate and propagate. Consequently, the prevalence of shear cracks appears to have increased. Within Group B, the B2 demonstrated improved damage resistance after the formation of the initial crack. The shift in the cracking mode pattern for groups C and group D is depicted in Fig. 11 (i–n). The results indicate that inserting GNPs into a hybrid fibre matrix significantly reduced the proportion of tensile cracks compared

to the reference specimen (R2). This implies that the hybridizing PVA-PO fibres, particularly in combination with GNPs, may influence crack propagation mechanisms.

4.4. Microstructure analysis

Fig. 12 presents the microstructural properties of reference specimens (R1 and R2), and the selected specimens from four different mix groups (A, B, C, and D), analysed by a VHX-7000 digital microscope. Larger close-ups of the test materials are depicted in Fig. 13 to better illustrate the effect of fibre distribution on micro-scale properties. The microstructure image of the plain GNPs-reinforced specimens (R2) revealed that GNP particles were wrapped within the hydration products in the cement matrix. This observation suggests that probe ultrasonication of GNPs combined with PCE dispersant effectively distributed GNPs throughout the cementitious composites without significant agglomeration. For Group B (B2 specimen), PVA fibres appeared uniformly distributed and in close contact with GNPs throughout the matrices, with no signs of fibre agglomeration. At higher magnifications (1000 μm and 25 μm), GNPs were observed adhering to the PVA fibre surfaces. This may indicate the formation of a denser interfacial network between PVA fibre and the matrix, thereby improving the interfacial properties. In contrast, PO fibres in Group A (A2 specimen) exhibited non-uniform distribution and localized agglomeration when combined with GNPs. This difference could be attributed to the smoother surface morphology of PO fibres, which may hinder interfacial bonding with wrinkled GNPs during mixing. The hybrid PO-PVA-GNPs (C2 specimen) showed a homogeneous microstructure with GNPs dispersed between PO and PVA fibres. This suggests that GNPs act as nano-reinforcements, potentially bridging gaps between fibres and cement matrices. Group D (specimen D2) displayed a denser interfacial microstructure when GNPs were combined with lower PO-PVA fibre ratios. This may reflect improved fibre dispersion and reduced agglomeration, possibly delaying microcrack propagation.

5. Conclusions

This study investigated the synergistic effects of GNPs with single and hybrid PO-PVA fibres at different dosages (0.1 %, 0.3 %, and 0.6 % by volume) on the fracture behaviour of concrete specimens, using acoustic emission technology for monitoring purposes. Based on the complex experimental results, the following conclusions can be drawn:

1) The substitution of GNPs in both single and hybrid PO-PVA fibre matrices appears to enhance interfacial bonding, microstructural integrity and fracture performance. This is supported by a notable increase in accumulated AE hits and the dominance of higher spectral frequency bands during both the pre-peak and post-peak phases. The most beneficial reinforcing effect of GNPs was observed in the C2 and D1 specimens, where balanced fibre dosages of PO and PVA may have resulted in stronger fibre-matrix

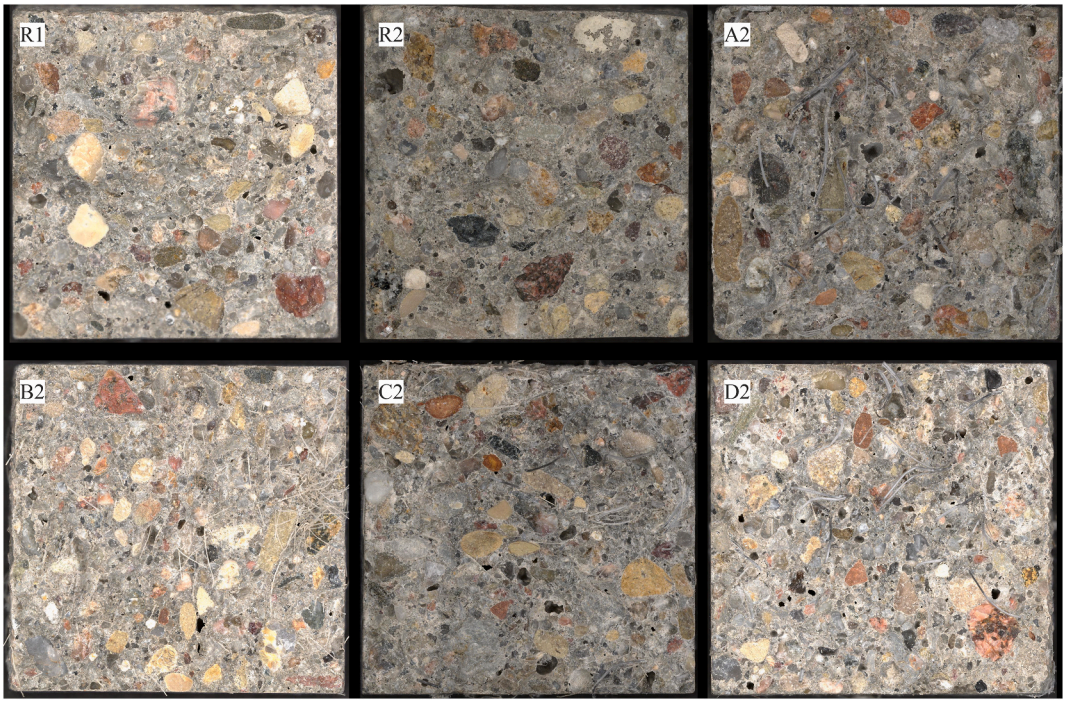

Fig. 12. Digital microstructure images of the plain concrete specimen (R1), plain GNPs-reinforced specimen (R2), and four specimens of various mix groups (A2 to D2).

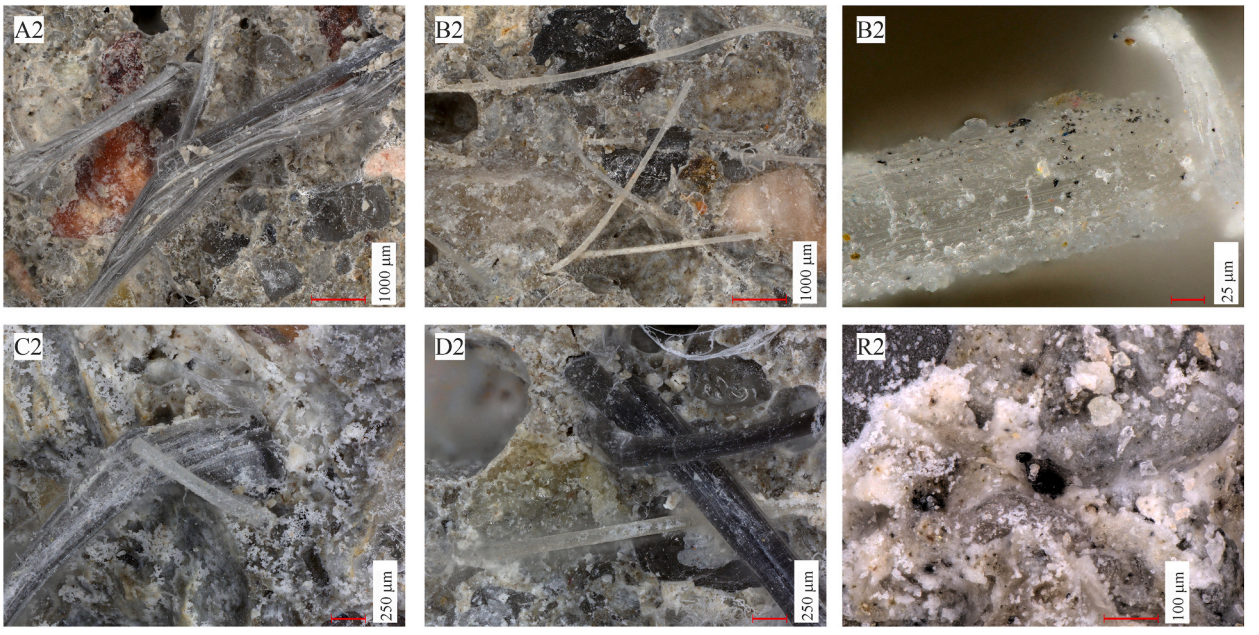

Fig. 13. Microscopic images at different-fold magnifications of plain GNPs-reinforced specimen (R2) and four specimens of various mixture groups (A2 to D2).

interactions, improved crack bridging, and a stable trend in cumulative AE hits. Conversely, higher PO content appears to have led to fibre agglomeration, potentially weakening the reinforcement effects and increasing microcracking activities.

2) The overall C-AE energy and Ib-value results suggest that appropriate combinations of PVA and PO fibres with GNPs may significantly improve interfacial bonding and crack resistance during both the initial and post-cracking phases. Specimens B2, C2 and D1 specimens exhibited higher cumulative AE energy and stable Ib-values during the post-peak cracking phase, indicating superior ductility and energy absorption capabilities.
3) AE intensity parameters, including the historical index (HI), and the logarithmic severity index $\log_{10}S_r$, suggest varying degrees of damage over time in the selected specimens. The B2, C2 and D1 specimens exhibited optimal performance, characterized by multiple discrete damage events during loading and step-wise increments in $\log_{10}S_r$ values. These configurations appear to outperform others in terms of controlled crack propagation and reduced overall damage severity. In contrast, specimens with higher HI and $\log_{10}S_r$ values, such as the D3 specimen, may have experienced more severe cracking. A safer zone analysis, which generated HI and S_r values at the point of material failure, supports the hypothesis that these specimens offered better resistance to damage and fracture.
4) RA and AF distribution analysis indicates that the GNPs influenced the crack propagation mechanism, with different fibre contents showing distinct trends in damage accumulation. The integration of GNPs with PO and PVA fibres appears to shift the main fracture type towards more widespread shear cracks, potentially indicating enhanced damage resistance. The hybridisation of PVA-PO-GNPs may have reduced the proportion of tensile cracks, suggesting a potential influence on the crack propagation mechanism.
5) Microstructure images suggest that the hybridisation of PO-PVA fibres with GNPs may enhance interfacial bonding between the fibres and the matrix. This could result in a denser and potentially stiffer matrix, which may improve crack bridging and energy absorption during microcrack propagation.

CRediT authorship contribution statement

Shahzad Ashraf: Writing – original draft, Visualization, Methodology, Investigation, Formal analysis, Conceptualization. **Magdalena Rucka:** Writing – review & editing, Visualization, Supervision, Project administration, Methodology, Investigation, Funding acquisition, Formal analysis, Conceptualization.

Declaration of competing interest

The authors declare that they have no known competing financial interests or personal relationships that could have appeared to influence the work reported in this paper.

Acknowledgements

The study was supported by the National Science Centre, Poland, project no. 2019/35/B/ST8/01905.

Data availability

Data will be made available on request.

References

[1] P.K. Mehta, P.J.M. Monteiro, Concrete: Microstructure, Properties, and Materials, fourth ed., McGraw-Hill Education, New York, 2014. https://www.accessengineeringlibrary.com/content/book/9780071797870.
[2] W. Li, B. Dong, Z. Yang, J. Xu, Q. Chen, H. Li, F. Xing, Z. Jiang, Recent advances in intrinsic self-healing cementitious materials, Adv. Mater. 30 (2018) e1705679, https://doi.org/10.1002/adma.201705679.
[3] A. Siddika, M.A. Al Mamun, W. Ferdous, R. Alyousef, Performances, challenges and opportunities in strengthening reinforced concrete structures by using FRPs – a state-of-the-art review, Eng. Fail. Anal. 111 (2020) 104480, https://doi.org/10.1016/j.engfailanal.2020.104480.
[4] G.L. Golewski, The phenomenon of cracking in cement concretes and reinforced concrete structures: the mechanism of cracks formation, causes of their initiation, types and places of occurrence, and methods of detection—a review, Buildings 13 (2023) 765, https://doi.org/10.3390/buildings13030765.
[5] C. Fu, N. Jin, H. Ye, X. Jin, W. Dai, Corrosion characteristics of a 4-year naturally corroded reinforced concrete beam with load-induced transverse cracks, Corros. Sci. 117 (2017) 11–23, https://doi.org/10.1016/j.corsci.2017.01.002.
[6] A. Blagojevic, The Influence of Cracks on the Durability and Service Life of Reinforced Concrete Structures in Relation to Chloride-Induced Corrosion, 2016.
[7] C. Aloupis, M.J. Chajes, H.W. Shenton III, Damage identification in cable-stayed bridges based on the redistribution of dead and thermal loads, Eng. Struct. 284 (2023) 115967, https://doi.org/10.1016/j.engstruct.2023.115967.
[8] J. Xiao, H. Liu, T. Ding, K. Yu, L. Zhang, X. Xiao, H. Zhu, Rebar-free concrete construction: concept, opportunities and challenges, J. Build. Eng. 86 (2024) 108933, https://doi.org/10.1016/j.jobe.2024.108933.
[9] F. He, L. Biolzi, V. Carvelli, P.J.M. Monteiro, Digital imaging monitoring of fracture processes in hybrid steel fiber reinforced concrete, Compos. Struct. 298 (2022) 116005, https://doi.org/10.1016/j.compstruct.2022.116005.
[10] M.M. Sherif, E.M. Khakimova, J. Tanks, O.E. Ozbulut, Cyclic flexural behavior of hybrid SMA/steel fiber reinforced concrete analyzed by optical and acoustic techniques, Compos. Struct. 201 (2018) 248–260, https://doi.org/10.1016/j.compstruct.2018.06.039.
[11] D. Liu, J. Yu, F. Qin, K. Zhang, Z. Zhang, Mechanical performance of high-strength engineering cementitious composites (ECC) with hybriding PE and steel fibers, Case Stud. Constr. Mater. 18 (2023) e01961, https://doi.org/10.1016/j.cscm.2023.e01961.
[12] J.-X. Lin, Y. Song, Z.-H. Xie, Y.-C. Guo, B. Yuan, J.-J. Zeng, X. Wei, Static and dynamic mechanical behavior of engineered cementitious composites with PP and PVA fibers, J. Build. Eng. 29 (2020) 101097, https://doi.org/10.1016/j.jobe.2019.101097.
[13] M.M. Moein, A. Saradar, K. Rahmati, Y. Rezakhani, S.A. Ashkan, M. Karakouzian, Reliability analysis and experimental investigation of impact resistance of concrete reinforced with polyolefin fiber in different shapes, lengths, and doses, J. Build. Eng. 69 (2023) 106262, https://doi.org/10.1016/j.jobe.2023.106262.
[14] Z. Yuan, Y. Jia, Mechanical properties and microstructure of glass fiber and polypropylene fiber reinforced concrete: an experimental study, Constr. Build. Mater. 266 (2021) 121048, https://doi.org/10.1016/j.conbuildmat.2020.121048.
[15] D. Liu, F. Qin, J. Di, Z. Zhang, Flexural behavior of reinforced concrete (RC) beams strengthened with carbon fiber reinforced polymer (CFRP) and ECC, Case Stud. Constr. Mater. 19 (2023) e02270, https://doi.org/10.1016/j.cscm.2023.e02270.
[16] X. Ou, G. Ye, J. Jiang, J. Gong, Z. He, Improving electrical and mechanical properties of cement composites by combined addition of carbon black and carbon nanotubes and steel fibers, Constr. Build. Mater. 438 (2024) 136931, https://doi.org/10.1016/j.conbuildmat.2024.136931.
[17] M. Ramezani, O.E. Ozbulut, M.M. Sherif, Mechanical characterization of high-strength and ultra-high-performance engineered cementitious composites reinforced with polyvinyl alcohol and polyethylene fibers subjected to monotonic and cyclic loading, Cem. Concr. Compos. 148 (2024) 105472, https://doi.org/10.1016/j.cemconcomp.2024.105472.
[18] H. Zhang, B. He, W. Chen, J. Ai, X. Zhu, Z. Jiang, Investigating the influence of fibre type and content on the toughness and ductility of geopolymer mortar with acoustic emission technology, Cem. Concr. Compos. 147 (2024) 105434, https://doi.org/10.1016/j.cemconcomp.2024.105434.
[19] M. Gorji Azandariani, M. Vajdian, K. Asghari, S. Mehrabi, Mechanical properties of polyolefin and polypropylene fibers-reinforced concrete–An experimental study, Composer Part C Open Access 12 (2023) 100410, https://doi.org/10.1016/j.jcomc.2023.100410.
[20] H.R. Pakravan, T. Ozbakkaloglu, Synthetic fibers for cementitious composites: a critical and in-depth review of recent advances, Constr. Build. Mater. 207 (2019) 491–518, https://doi.org/10.1016/j.conbuildmat.2019.02.078.
[21] A. Noushini, M. Hastings, A. Castel, F. Aslani, Mechanical and flexural performance of synthetic fibre reinforced geopolymer concrete, Constr. Build. Mater. 186 (2018) 454–475, https://doi.org/10.1016/j.conbuildmat.2018.07.110.
[22] A. Noushini, B. Samali, K. Vessalas, Effect of Polyvinyl Alcohol (PVA) Fibre on Dynamic and Material Properties of Fibre Reinforced Concrete, vol. 49, 2013, pp. 374–383, https://doi.org/10.1016/j.conbuildmat.2013.08.035.
[23] J. Qiu, X.N. Lim, E.-H. Yang, Fatigue-induced in-situ strength deterioration of micro-polyvinyl alcohol (PVA) fiber in cement matrix, Cem. Concr. Compos. 82 (2017) 128–136, https://doi.org/10.1016/j.cemconcomp.2017.06.002.
[24] M.G. Alberti, A. Enfedaque, J.C. Gálvez, On the mechanical properties and fracture behavior of polyolefin fiber-reinforced self-compacting concrete, Constr. Build. Mater. 55 (2014) 274–288, https://doi.org/10.1016/j.conbuildmat.2014.01.024.
[25] S. Das, M. Habibur Rahman Sobuz, V.W.Y. Tam, A.S.M. Akid, N.M. Sutan, F.M.M. Rahman, Effects of incorporating hybrid fibres on rheological and mechanical properties of fibre reinforced concrete, Constr. Build. Mater. 262 (2020) 120561, https://doi.org/10.1016/j.conbuildmat.2020.120561.
[26] S.H. Chu, Strain-hardening ultra-high performance concrete (UHPC) with hybrid steel and ultra-high molecular weight polyethylene fibers, Constr. Build. Mater. 438 (2024) 136716, https://doi.org/10.1016/j.conbuildmat.2024.136716.
[27] E.R.K. Chandrathilaka, S.K. Baduge, P. Mendis, P.S.M. Thilakarathna, Structural applications of synthetic fibre reinforced cementitious composites: a review on material properties, fire behaviour, durability and structural performance, Structures 34 (2021) 550–574, https://doi.org/10.1016/j.istruc.2021.07.090.
[28] E. Gurbuz, S. Erdem, M. Zhang, Static and impact performance of engineered cementitious composites with hybrid graphite nano platelets modified PVA and shape memory alloy fibres, J. Build. Eng. 92 (2024) 109776, https://doi.org/10.1016/j.jobe.2024.109776.
[29] H. Xu, Z. Shao, Z. Wang, L. Cai, Z. Li, H. Jin, T. Chen, Experimental study on mechanical properties of fiber reinforced concrete: effect of cellulose fiber, polyvinyl alcohol fiber and polyolefin fiber, Constr. Build. Mater. 261 (2020) 120610, https://doi.org/10.1016/j.conbuildmat.2020.120610.
[30] I.G. Shaaban, M. Said, S.U. Khan, M. Eissa, K. Elrashidy, Experimental and theoretical behaviour of reinforced concrete beams containing hybrid fibres, Structures 32 (2021) 2143–2160, https://doi.org/10.1016/j.istruc.2021.04.021.
[31] S. Yao, C. Hu, F. Wang, S. Hu, Improving the interfacial properties of PVA fiber and cementitious composite: design and characterization, Constr. Build. Mater. 409 (2023) 134163, https://doi.org/10.1016/j.conbuildmat.2023.134163.
[32] M. Lu, H. Xiao, M. Liu, J. Feng, Carbon fiber surface nano-modification and enhanced mechanical properties of fiber reinforced cementitious composites, Constr. Build. Mater. 370 (2023) 130701, https://doi.org/10.1016/j.conbuildmat.2023.130701.
[33] M.Ç. Tüzemen, F. Khakzad, E. Salamci, Investigation of tensile properties of glass fiber/epoxy nanocomposites laminates enhanced with graphene nanoparticles, Fibers Polym. 22 (2021) 1441–1448, https://doi.org/10.1007/s12221-021-0521-0.

[34] S.N. Hosseini Abbandanak, M. Abdollahi Azghan, A. Zamani, M. Fallahnejad, R. Eslami-Farsani, H. Siadati, Effect of graphene on the interfacial and mechanical properties of hybrid glass/Kevlar fiber metal laminates, J. Ind. Text. 51 (2022) 2576S–2593S, https://doi.org/10.1177/1528083720932222.
[35] M. Cao, S. Wang, J. Zang, M. Liu, C. Qian, Y. Zhang, D. Na, Experimental and simulation analysis of the effect of GNPs on the mechanical and interfacial properties of CF/PEEK-Ti fiber metal laminates, Compos. Sci. Technol. 246 (2024) 110387, https://doi.org/10.1016/j.compscitech.2023.110387.
[36] G.B. Berti, D. Piazza, B.F. Bortoli, R.N. Brandalise, Enhancing polypropylene composites: synergistic effects of graphene nanoplatelets and glass fibers on mechanical and thermal properties, J. Nanoparticle Res. 26 (2024) 154, https://doi.org/10.1007/s11051-024-06060-w.
[37] D. De Cicco, Z. Asaee, F. Taheri, Use of nanoparticles for enhancing the interlaminar properties of fiber-reinforced composites and adhesively bonded joints—a review, Nanomaterials 7 (2017) 360, https://doi.org/10.3390/nano7110360.
[38] S. Ashraf, M. Rucka, Microcrack monitoring and fracture evolution of polyolefin and steel fibre concrete beams using integrated acoustic emission and digital image correlation techniques, Constr. Build. Mater. 395 (2023), https://doi.org/10.1016/j.conbuildmat.2023.132306.
[39] A. Dev, M. Chellapandian, S.S. Prakash, Y. Kawasaki, Failure-mode analysis of macro-synthetic and hybrid fibre-reinforced concrete beams with GFRP bars using acoustic emission technique, Constr. Build. Mater. 249 (2020) 118737, https://doi.org/10.1016/j.conbuildmat.2020.118737.
[40] J. Xu, S. Ashraf, S. Khan, X. Chen, A. Akbar, F. Farooq, Micro-cracking pattern recognition of hybrid CNTs/GNPs cement pastes under three-point bending loading using acoustic emission technique, J. Build. Eng. 42 (2021) 102816, https://doi.org/10.1016/j.jobe.2021.102816.
[41] A.A. Abouhussien, A.A.A. Hassan, Classification of damage in self-consolidating rubberized concrete using acoustic emission intensity analysis, Ultrasonics 100 (2020) 105999, https://doi.org/10.1016/j.ultras.2019.105999.
[42] M.N. Noorsuhada, An overview on fatigue damage assessment of reinforced concrete structures with the aid of acoustic emission technique, Constr. Build. Mater. 112 (2016) 424–439, https://doi.org/10.1016/j.conbuildmat.2016.02.206.
[43] F. Zhang, Y. Yang, S.A.A.M. Fennis, M.A.N. Hendriks, Developing a new acoustic emission source classification criterion for concrete structures based on signal parameters, Constr. Build. Mater. 318 (2022) 126163, https://doi.org/10.1016/j.conbuildmat.2021.126163.
[44] P.R. Prem, A.R. Murthy, Acoustic emission monitoring of reinforced concrete beams subjected to four-point-bending, Appl. Acoust. 117 (2017) 28–38, https://doi.org/10.1016/j.apacoust.2016.08.006.
[45] A.A. Abouhussien, A.A.A. Hassan, Assessment of crack development in engineered cementitious composites based on analysis of acoustic emissions, J. Mater. Civ. Eng. 31 (2019), https://doi.org/10.1061/(ASCE)MT.1943-5533.0002690.
[46] J. Li, J. Yan, G. Xue, J. Niu, Acoustic emission behavior of polyvinyl alcohol (PVA) fiber reinforced calcium sulphoaluminate cement mortar under flexural load, J. Build. Eng. 40 (2021) 102734, https://doi.org/10.1016/j.jobe.2021.102734.
[47] A.H. Korayem, N. Tourani, M. Zakertabrizi, A.M. Sabziparvar, W.H. Duan, A review of dispersion of nanoparticles in cementitious matrices: nanoparticle geometry perspective, Constr. Build. Mater. 153 (2017) 346–357, https://doi.org/10.1016/j.conbuildmat.2017.06.164.
[48] L.J. Jaramillo, R. Kalfat, Fresh and hardened performance of concrete enhanced with graphene nanoplatelets (GNPs), J. Build. Eng. 75 (2023) 106945, https://doi.org/10.1016/j.jobe.2023.106945.
[49] K. Ohno, M. Ohtsu, Crack classification in concrete based on acoustic emission, Constr. Build. Mater. 24 (2010) 2339–2346, https://doi.org/10.1016/j.conbuildmat.2010.05.004.
[50] J. Geng, Q. Sun, Y. Zhang, L. Cao, W. Zhang, Studying the dynamic damage failure of concrete based on acoustic emission, Constr. Build. Mater. 149 (2017) 9–16, https://doi.org/10.1016/j.conbuildmat.2017.05.054.
[51] D.G. Aggelis, D.V. Soulioti, N. Sapouridis, N.M. Barkoula, A.S. Paipetis, T.E. Matikas, Acoustic emission characterization of the fracture process in fibre reinforced concrete, Constr. Build. Mater. 25 (2011) 4126–4131, https://doi.org/10.1016/j.conbuildmat.2011.04.049.
[52] A. Nair, C.S. Cai, Acoustic emission monitoring of bridges: review and case studies, Eng. Struct. 32 (2010) 1704–1714, https://doi.org/10.1016/j.engstruct.2010.02.020.
[53] H. Zhang, B. He, X. Zhu, Q. Wang, Z. Jiang, Flexural performance and patterns identification of UHPC subjected to alternating elevated and cryogenic attacks with acoustic emission characterization, Constr. Build. Mater. 364 (2023) 129962, https://doi.org/10.1016/j.conbuildmat.2022.129962.
[54] Z. Wang, K. Ding, H. Ren, J. Ning, Quantitative acoustic emission investigation on the crack evolution in concrete prisms by frequency analysis based on wavelet packet transform, Struct. Health Monit. 21 (2022) 1046–1060, https://doi.org/10.1177/14759217211018871.
[55] P.R. Prem, M. Verma, P.S. Ambily, Damage characterization of reinforced concrete beams under different failure modes using acoustic emission, Structures 30 (2021) 174–187, https://doi.org/10.1016/j.istruc.2021.01.007.
[56] D.G. Aggelis, Classification of cracking mode in concrete by acoustic emission parameters, Mech. Res. Commun. 38 (2011) 153–157, https://doi.org/10.1016/j.mechrescom.2011.03.007.
[57] S. Shahidan, R. Pulin, N. Muhamad Bunnori, K.M. Holford, Damage classification in reinforced concrete beam by acoustic emission signal analysis, Constr. Build. Mater. 45 (2013) 78–86, https://doi.org/10.1016/j.conbuildmat.2013.03.095.
[58] Z.-H. Zhang, J.-H. Deng, A new method for determining the crack classification criterion in acoustic emission parameter analysis, Int. J. Rock Mech. Min. Sci. 130 (2020) 104323, https://doi.org/10.1016/j.ijrmms.2020.104323.